Received: 25 November 2018 | Revised: 29 January 2019 | Accepted: 2 March 2019

DOI: 10.1002/gj.3516

RESEARCH ARTICLE

WILEY

The genesis of gold deposits in the Hetai goldfield, South China: New constraints from geochronology, fluid inclusion, and multiple isotopic studies

Lixing Wang[1,2] | Zhaoxia Zhao[1,2] | Qinyi Huang[1,2] | Deru Xu[3] | Qianqian Jiao[4] | Genwen Chen[1] | Jianxin Cai[5] | Shaohao Zou[1,2] | Teng Deng[3] | Qiang Shan[1]

[1] Key Laboratory of Mineralogy and Metallogeny, Guangzhou Institute of Geochemistry, Chinese Academy of Sciences, Guangzhou, China

[2] University of Chinese Academy of Sciences, Beijing, China

[3] State Key Laboratory of Nuclear Resources and Environment, East China University of Technology, Nanchang, China

[4] Department of Earth Sciences, Kunming University of Science and Technology, Kunming, China

[5] Key Laboratory of Ocean and Marginal Sea Geology, South China Sea Institute of Oceanology, Chinese Academy of Sciences, Guangzhou, China

Correspondence
Deru Xu, State Key Laboratory of Nuclear Resources and Environment, East China University of Technology, Nanchang 330013, China.
Email: xuderu@gig.ac.cn

Funding information
China Geological Survey, Grant/Award Number: 12120114052801; National Natural Science Foundation of China, Grant/Award Number: 41472171; National Key R&D Program of China, Grant/Award Number: 2016YFC0600401

Handling Editor: L. Tang

The Hetai goldfield is one of the largest gold mining districts in the South China Block. A complex paragenesis consists of three mineralization stages: syntectonic metamorphic stage, hydrothermal stage, and supergene stage. The syntectonic metamorphic stage is characterized by banded quartz (Q1) and invisible Au in mylonites. The hydrothermal stage, which is the main gold mineralization stage, can be divided into three substages: an early substage characterized by coarse-grained quartz (Q2) + pyrite + arsenopyrite + pyrrhotite, an intermediate substage characterized by gray fine-grained quartz (Q3) + electrum + poly-sulphides + sericite + chlorite and a late substage with predominate white quartz (Q4) + calcite as well as lesser sulphides. During the supergene stage, malachite, covellite, and limonite were formed. Four types of fluid inclusions (FIs) in these types of quartz were identified: aqueous FIs (type 1), CO_2-bearing aqueous FIs (type 2), CO_2-rich FIs (type 3), and solid-bearing FIs (type 4). Q1 only contains type 1 FIs; Q2 contains types 2 and 4 FIs; Q3 contains types 2 and 3 FIs; and Q4 only contains type 1 FIs. Microthermometric results show that the homogenization temperatures of fluid inclusions range from 350°C to 400°C for Q1, 250°C to 320°C for Q2, 138°C to 245°C for Q3, and 110°C to 207°C for Q4. Salinities of fluid inclusions range from 3.4 to 5.7 wt.%, 2.6 to 12.9 wt.%, 0.5 to 11.5 wt.%, and 0.2 to 7.3 wt.% for Q1, Q2, Q3, and Q4, respectively. Alteration minerals (sericite and chlorite) from the main mineralization stage have $\delta D_{H_2O\text{-}VSMOW}$ values of −62‰ to −98‰ and calculated $\delta^{18}O_{H_2O\text{-}VSMOW}$ values of 6.3‰ to 4.4‰. The in situ sulphur isotope analysis of pyrite yields a narrow $\delta^{34}S_{CDT}$ range of −1.5‰ to −5.2‰ (average −3.4‰), combined with the Pb isotopic compositions of the sulphides, wall rocks, and Wucun pluton, revealing that the ore-forming material was mainly derived from magmatic source. The mineralization age (sericite $^{40}Ar/^{39}Ar$: 159.3 ± 0.8 Ma) is close to the emplacement age of Wucun biotite monzonitic granite pluton (LA-ICP-MS zircon U–Pb age: 158.1 ± 1.9 Ma). These geochemical and geochronological data suggest that the main phase of gold mineralization in the Hetai goldfield is genetically related to the granitic activities in the Late Jurassic rather than the mylonitization event in the Late Triassic to Early Jurassic.

KEYWORDS

auriferous mylonitic zone, fluid inclusions, geochronology, Hetai goldfield, H–O–S–Pb isotopes

1 | INTRODUCTION

The Hetai goldfield is one of the largest gold mining districts in the Qin–Hang metallogenic belt, South China (Figure 1). The ore bodies in this goldfield mainly occur along a series of ductile shear zones with mylonitization (J. X. Cai, 2012; J. Chen & Wang, 1994; Duan, He, & Zhou, 1992; S. He, Duan, Zhou, & Peng, 1992; H. N. Wang, Chen, Ji, & Qu, 1997; G. L. Zhang, Boulter, & Liang, 2001). Many metallogenic models have been proposed in the Hetai goldfield, and the central concern is the relationship between the auriferous mineralization and the mylonitization along the ductile shear zones. Some researchers (J. X. Cai, 2012; Duan et al., 1992; S. He et al., 1992; Zeng, 1986; Y. Zheng et al., 2014) thought that the mineralization is coeval with ductile shearing and thus proposed the mineralization was formed in the Late Indosinian Orogeny to Early Yanshanian based on the muscovite $^{40}Ar/^{39}Ar$ age data from the ductile shear zones (213–187 Ma; J. X. Cai, 2012; K. J. Zhang & Cai, 2009). Consequently, the model suggests that the ore-forming fluids as well as Au were mainly released from the wall rocks (the Yunkai Group) during the mylonitization event (W. He, 1993; Lu, 1993; H. N. Wang et al., 1989; Y. Zheng et al., 2014; Y. Z. Zhou, Zhang, Lu, Guha, & Chown, 1995). Other workers, on the other hand, argued that the auriferous mineralization occurred after the ductile shear deformation and is related to magmatic activities in the Yanshanian Orogeny (Jiao, Wang, et al., 2017; C. Wang, Zhang, Wang, Qiu, & Gong, 2012; Zhai et al., 2006). This is mainly based on observations that the H–O isotope compositions in quartz from ores and fluid inclusions plot in the field of magmatic water (Jiao, Wang, et al., 2017; Tu & Gao, 1991; H. N. Wang et al., 1997; Ye & Qiu, 1993) and that the emplacement age of the Wucun granitic pluton adjacent to the mineralization (magmatic zircon U–Pb: 153.6 ± 2.1 Ma; Zhai, Yuan, Li, & Huang, 2005) is broadly the same as the mineralization ages (hydrothermal zircon U–Pb: 152.5 ± 3.1 Ma; Zhai et al., 2006). The key to resolve these disputes lies in tracing the origins of the ore-forming constituents and obtaining more reliable ages.

Albeit immense works have been done on fluid inclusions and isotopes, the majority of those results are not convincing due to lack of systematic studies, and thus, puzzles are still pending. For example, based on gas and liquid components of the fluid inclusions in quartz in the ores, the mineralization fluids were regarded as being dominated by low-salinity CO_2-bearing hydrothermal fluids, resembling a metamorphic origin; thus, the Hetai goldfield was considered as typical

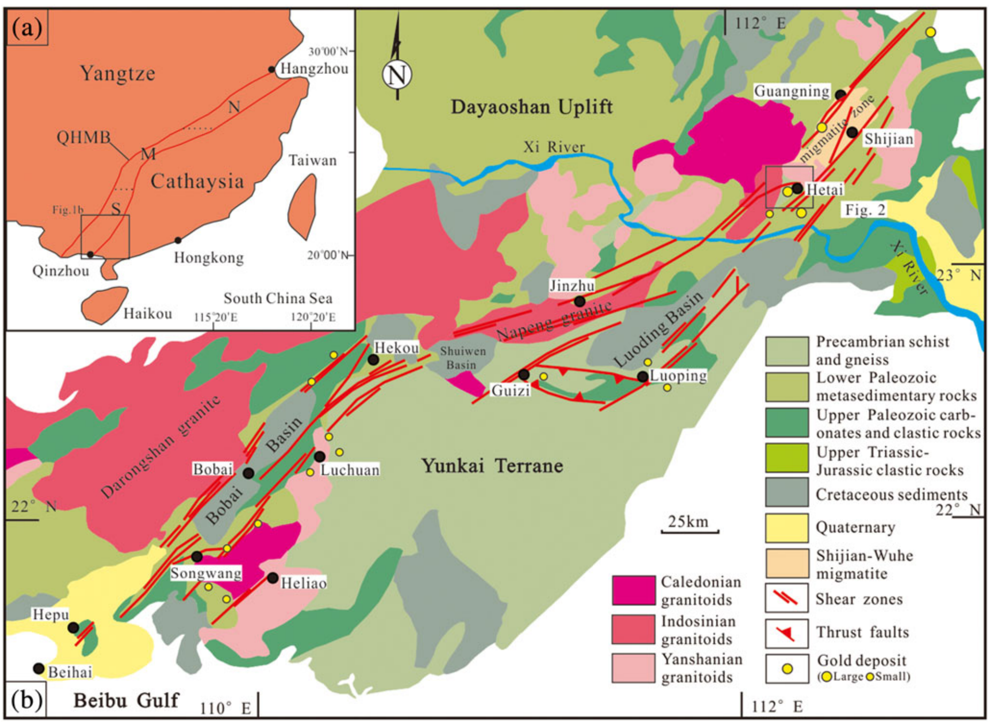

FIGURE 1 (a) Tectonic framework of the South China Block showing the location of the Qinzhou Bay–Hangzhou Bay Metallogenic Belt; "N," "M," and "S" represent the northern, middle, and southern segments of the QHMB, respectively (modified from Y. Z. Zhou et al., 2012). (b) Geological map of the Guangning–Bobai shear zone and its adjacent areas showing structures, strata, and magmatic rocks (modified from GBGMR, 1988). The locations of gold deposits are from (M. Cai, Zhan, Peng, Meng, & Liu, 2002). For clarity, other faults are not shown [Colour figure can be viewed at wileyonlinelibrary.com]

orogenic gold mineralization (Y. Zheng et al., 2014; Y. Z. Zhou et al., 1995). However, these characteristics of the ore-forming fluids are also found in intrusion-related gold systems (Baker & Lang, 2001; Hart, 2007). In addition, the previous fluid inclusion studies lacked detailed descriptions on the relationship between fluid inclusions and mineralization stages. Moreover, the unclear generation relationship even affected the results of H–O isotopic analyses that commonly blend different mineralizing stages of inclusions and thus derive a mixed nature for ore-forming fluids between metamorphic, magmatic, and meteoric origins (W. He, 1993; Jiao, Wang, et al., 2017; W. Liu, Huang, & Ouyang, 2005; Lu, 1993; Tu & Gao, 1991; H. N. Wang et al., 1989, 1997; Ye & Qiu, 1993). The same situation also complicates the S isotope data obtained from the bulk analytical methods, which may include sulphides from different generations. Furthermore, the mineralization time of the Hetai goldfield and the emplacement age of the Wucun pluton have also been debated due to the shortage of robust isotope ages. Zhai et al. (2005, 2006) conducted isotopic dilution method and SHRIMP zircon U–Pb dating on hydrothermal zircon from different auriferous quartz veins, yielding Early Caledonian (492 ± 16 Ma) and Yanshanian (153.6 ± 2.1 Ma) ages, respectively. Other emplacement ages (210 ± 69 Ma; G. Y. Wu, 1986; 125.6 ± 57 Ma; L. Wang et al., 2003) have also been obtained for the Wucun granitic pluton using the Rb–Sr whole-rock isochron method. Subsequently, Zhai et al. (2006) proposed a zircon U–Pb age of 152.5 ± 3.1 Ma for the Wucun granite by the isotopic dilution method, but only four zircons data that deviate from the concordia were obtained. Further, lack of descriptions on the zircon morphology and texture makes the interpretation of these U–Pb ages ambiguous. Therefore, further study is required to properly constrain the genesis of the Hetai goldfield.

This study is aimed at tracing the origin(s) of the ore-forming fluids and components for achieving a better understanding on genesis of the Hetai goldfield, with regard to shear deformation and magmatism. Fluid inclusions were studied in quartz clearly assigned to different mineralization stages based on detailed petrography. In order to avoid the problems encountered in H–O isotope analyses with the traditional fluid inclusion method, we analysed the H–O isotopes of mineralization-related hydrous minerals (e.g., mica and chlorite). In addition, in situ measurement of S isotopes was conducted on pyrite formed in the hydrothermal mineralization stage, and the whole-rock Pb isotopes of strata, migmatite, and granite were then analysed to provide constraints for the sources of metals. Furthermore, new $^{40}Ar/^{39}Ar$ dating of sericite from the ores and LA-ICP-MS zircon U–Pb dating of the Wucun granite were conducted. Finally, the ore genesis of the Hetai goldfield discussed by integrating all the new data obtained in this study and previously published ones.

2 | GEOLOGICAL SETTING

The Qin–Hang metallogenic belt (QHMB) is one of most important metallogenic belts in South China (Figure 1a). Geotectonically, the QHMB covers the range of the Qinzhou Bay–Hangzhou Bay Juncture Orogenic Belt, which has been interpreted as a giant tectonic suture between the Yangtze and Cathaysia blocks of South China, and has experienced multiple phases of tectonic disturbances associated with numerous metal deposits of various scales, including one rifting event in the Neoproterozoic and several tectonic events in the Phanerozoic, such as Caledonian, Indosinian, and Yanshanian orogenies (Jiao, Deng, et al., 2017; Z. X. Li et al., 2010; Pirajno & Bagas, 2002; Shu, Faure, Yu, & Jahn, 2011; L. Wang et al., 2003; G. W. Zhang et al., 2013). The QHMB can be divided into the northern (N), middle (M), and southern (S) sections (Figure 1a), which are endowed with the predominant mineral resources of Cu–Fe, W–Sn, and Au–Ag, respectively (Mao, Cheng, Chen, & Pirajno, 2013; Y. Z. Zhou et al., 2012).

The southern section of the QHMB comprises the Dayaoshan Uplift to the northwest and the Yunkai Terrane to the southeast, which are separated by the Guangning–Bobai shear fault belt (Figure 1b). The Hetai goldfield is situated in the north-eastern part of the Yunkai Terrane, which lithostratigraphically comprises a metamorphic basement and a sedimentary cover. The metamorphic basement is composed of the Gaozhou Complex and Yunkai Group, which were formed coevally in Late Neoproterozoic to Early Palaeozoic, whereas the sedimentary cover consists of weak to unmetamorphosed Ordovician to Cretaceous successions (Wan et al., 2010; Y. Wang, Fan, Zhao, Ji, & Peng, 2007). Locally, the Yunkai Group is dominated by gneisses, which have a Caledonian metamorphic age (ca. 440 Ma; Wan et al., 2010; Y. Wang, Wu, et al., 2012). The Upper Palaeozoic successions have an unconformable contact with the Yunkai Group, but this contact has been commonly reworked by late folding or ductile shearing (Y. Wang, Fan, Zhao, et al., 2007). These Upper Palaeozoic sediments are in turn uncomfortably overlain by the Upper Triassic to Lower Jurassic sandstones and conglomerates. The Cretaceous red beds, which were deposited in the Luoding, Shuiwen, and Bobai basins from northeast to southwest, uncomfortably overlie the pre-Cretaceous rocks. Voluminous Caledonian, Indosinian, and Yanshanian granitoids (GBGMR, 1988; S. B. Peng, Jin, Liu, et al., 2006; S. B. Peng, Wang, Wei, Peng, & Liang, 2006; Wan et al., 2010; Y. Wang, Fan, Cawood, et al., 2007; Zhai et al., 2005) occur on the north-western flank of the Yunkai Terrane and roughly show a NE-trending distribution (Figure 1b).

The Hetai goldfield occurs within a regional first-order fault zone, called the Guangning–Bobai Fault. The fault zone shows a broad sinuous shape trending NE–SW for more than 500 km with widths of 30–60 km (Figure 1b; J. X. Cai, 2013). The general trend in the northern (Guangning and Hetai) and southern (Luchuan and Songwang) segments of the fault zone is N45°E, which mainly consists of several approximately parallel shear zones, while the middle segment (Jinzhu) has a N60–70°E trend. Several subordinate shear zones with trends deviating from the main shear zones are also present, such as the N60–70°E shear zone in the Hetai goldfield and the NNE-trending ones in the Shijian town. These shear zones are highlighted by the strong ductile shear deformation and mylonitization in a variety of rocks including the Yunlougang granitic pluton (zircon U–Pb: 242–209 Ma; L. Wang et al., 2003), migmatites (zircon U–Pb: 240 ± 4 Ma; Zhai et al., 2006), Yunkai Group high-grade metamorphic rocks and associated Palaeozoic metasedimentary rocks in the Hetai goldfield (B. Y. Zhang & Yu, 1992), the Napeng granitic pluton in the Jinzhu area (zircon U–Pb: 205 ± 2 Ma; B. X. Peng, Wang, Fan, Peng, & Liang, 2006), the Yunkai Group in the Hekou area and the Darongshan granitic batholith (zircon U–Pb: 230–260 Ma; C. H. Chen, Hsieh, Lee, & Zhou, 2011), and Early Palaeozoic metasedimentary rocks in the Bobai area. The Guangning–Bobai shear fault belt, which probably formed during 213–187 Ma, displays dextral strike-slip features (J. X. Cai, 2012, 2013; Lin, Wang, & Chen, 2008; G. L. Zhang et al., 2001; K. J. Zhang & Cai, 2009). Mylonitic bands ranging in width from metres to decametres were well developed within these shear zones, and stretching along their strike can reach a few kilometres (Z. Q. Zhong, Zhou, & You, 1997). A large number of gold ore deposits are distributed along the Guangning–Bobai shear belt, but large gold deposits generally located in the north segment, such as the Hetai goldfield and the Xinzhou, Huangnikeng, and Changkeng gold deposits (Figure 1b; M. Cai et al., 2002).

3 | GEOLOGY OF THE HETAI GOLDFIELD

The Hetai goldfield is seated in the southern segment of the QHMB where the belt traverses the Dayaoshan anticlinorium, belonging to the nearly W-E-trending Mesozoic Nanling uplift belt (X. M. Zhou, Shen, Shu, & Niu, 2006). The main host rocks of the Hetai goldfield are the Neoproterozoic to Early Palaeozoic Yunkai Group (Au: 14.7 to 12.45 ppb), including mica-quartz schists, feldspar-mica schists and mica gneisses (Wan et al., 2010; G. L. Zhang et al., 2001). Early Palaeozoic sedimentary sequences are distributed to the southeast of the goldfield and consist of shallow to unmetamorphosed clastic rocks of the Ordovician (Au: 4.1 ppb) and Silurian (Au: 2.3 ppb). The contact relationship between the Neoproterozoic and Palaeozoic formations is presumably unconformable, but is blurred by later tectonic disturbances manifested as the Baoyatang–Kengwei Fault (F1 in Figure 2) moderately to steeply dipping to north (H. N. Wang et al., 1997; G. L. Zhang et al., 2001). The region is intruded by the Yunlougang medium-grained biotite granite pluton in the northwest and by the Wucun biotite monzonitic granite in the northeast (L. Wang et al., 2003; Zhai et al., 2005). Indosinian migmatites also commonly occur as isolated enclaves in the schist of the Yunkai Group, which locally coexist with pegmatite veins with thicknesses of 0.3–1 m (Figure 4a; L. Wang et al., 2003; Zhai et al., 2006).

Eight gold deposits have been discovered in the Hetai goldfield since 1982, including the Hehai, Houjing, Gaocun, Yunxi, Shangtai, Kengwei, Taozishan, and Taipingding deposits (Figure 2). Among these, the Gaocun, Yunxi, and Hehai deposits contribute to most of Au reserves. Up to now, the Hetai goldfield has produced 51.65 tonnes of gold at an average grade of 7.19 g/t, 7.58 tonnes of silver at 5.9 g/t (7 sample average) and 6.72 tonnes of copper at 0.22% (GGB, 2016; S. L. Wang, 2000).

3.1 | Characteristics of the orebodies

Most of the gold deposits in the Hetai orefield are controlled by a series of secondary shear fault zones with striking of N60–70°E cutting the Yunkai Group within the Guangning–Baobai fault zone. Nearly one hundred shear zones with mylonitization have been outlined, and individual zones have widths varying from tens of centimetres to tens of metres and lengths ranging from tens to hundreds of metres and even more than 1 km. Auriferous orebodies in the Hetai goldfield are mainly hosted parallel within the mylonitic zones (Figures 3 and 4b). The orebodies occur as steep veins with average thicknesses of 1.6–2.4 m and show various styles. For example, the No. 11 mylonite zone, which hosts the Gaocun deposit, is 40 m wide and 450 m long and strikes N70°E and dips to the NNW at angles of 65°–85°

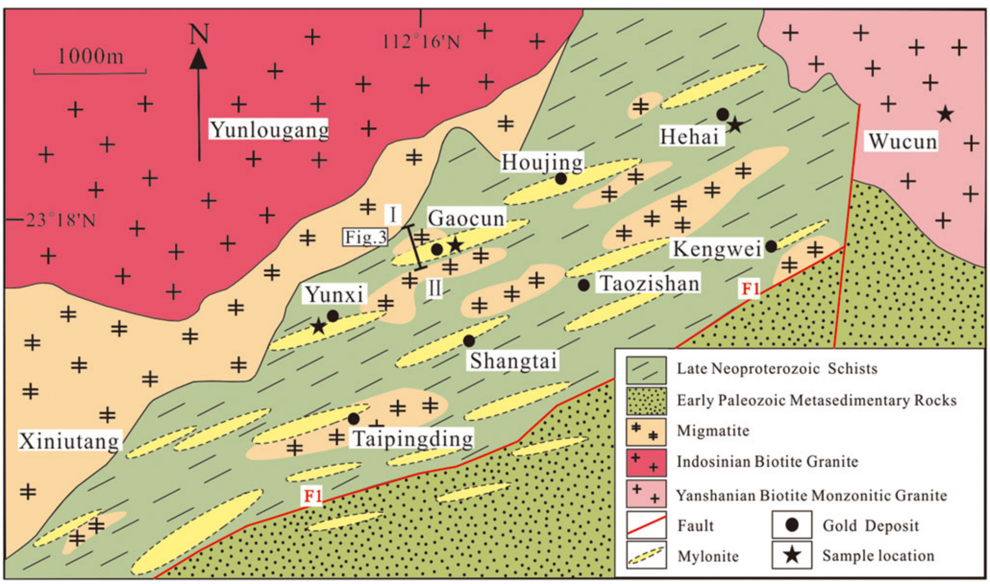

FIGURE 2 Simplified geologic map of the Hetai goldfield (modified from Fu, 1988; G. L. Zhang et al., 2001) [Colour figure can be viewed at wileyonlinelibrary.com]

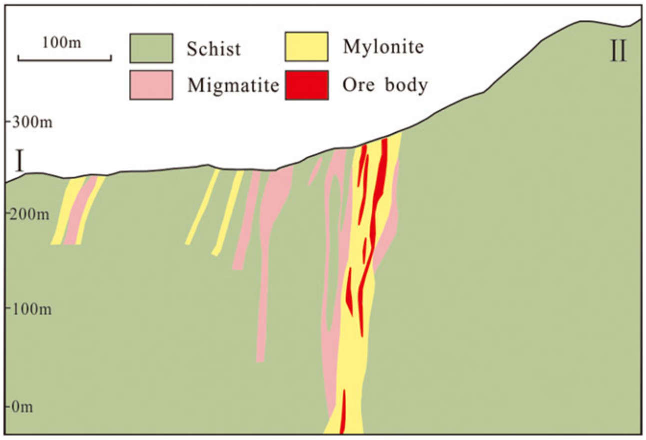

FIGURE 3 Geologic cross section of I-II orebodies at the Gaocun deposit (modified from GGB, 2016) [Colour figure can be viewed at wileyonlinelibrary.com]

(Figure 3). In plan view, these shear zones show left-step en-echelon arrangement indicating formation in dextral shearing. The orebodies mainly occur as silicified mylonites and silicified cataclasite and minor quartz veins. Auriferous silicified mylonites with elevated Au contents (0.2–0.7 g/t) are distinct from non-auriferous mylonites that have background Au value (5.8–7.8 ppb) of regional metamorphic rocks (Figure 4b). Au contents are positively related to the degree of silicification. Silicified cataclasite is controlled by brittle fractures and has significantly higher Au contents (15.5–194.5 g/t; Figure 4c). Auriferous veinlets in this type of orebodies occur either parallel or oblique to mylonitic foliations (Figure 4d). Both silicified mylonite and cataclasite types dominate the Gaocun and Yunxi deposits. Quartz-vein style of mineralization (0.2 g/t) occurs along the mylonitic foliations, mostly in the Hetai deposit, and few in the Gaocun deposit. In the Yunxi deposit, Au locally enriches to form bonanzas with average grades of 35–75 g/t and up to 593.06 g/t (S. L. Wang, 2000).

3.2 | Ore types and ore mineral assemblages

Three ore styles occur in the Hetai goldfield and roughly correspond to the three types of orebodies. The first style of ore is the auriferous altered mylonite, which is characterized by lamellar pyrites aligned parallel or subparallel to mylonitic foliations comprising preferentially orientated quartz (Q1) and mica (Figure 5a, b). The second ore style is the massive auriferous quartz vein comprising white coarse quartz grains (Q2; 0.5 to 1 cm) with mosaic contact, which also include relatively small-size white quartz locally coexisting with sulphides (Figure 5c–f). The third ore style is auriferous silicified cataclasite comprising sulphides filling the interstices of smoky gray quartz (Q3; 50 to 200 μm cross) or of white quartz (Q4) and calcite (Figure 5g–l).

The styles of ores in the Hetai goldfield have common assemblages of ore and gangue minerals. Primary ore minerals include electrum (88–91 at% Au), pyrite, pyrrhotite, chalcopyrite, and arsenopyrite, with minor siderite, tetradymite, galena, and sphalerite. The gangue minerals are mostly quartz, chlorite, and calcite with less mica and pyrophyllite. Only auriferous silicified cataclastic ores contain electrum occurring along fissures cutting or in interstices among quartz crystals, or in pyrrhotite, whereas the most common in the chalcopyrite grains (Figures 6), which is consistent with a positive correlation of Au and Cu concentrations in the Hetai goldfield (Figure 7).

3.3 | Mineralization stages and alteration

The Hetai goldfield has undergone three stages of mineralization based on mineral assemblages and crosscutting relationships. From early to late, these mineralizing stages are (1) syntectonic metamorphic stage, (2) hydrothermal stage associated with brittle deformation, and (3) supergene stage near the surface (Figure 8). The mineralization in the syntectonic metamorphic stage is evidenced by lamellar or veinlet-disseminated sulphides occurring along mylonitic foliations consisting of preferred orientation of minerals such as quartz (Q1), muscovite, and sericite (Figure 5a,b). This stage produced ores of auriferous altered mylonite type with invisible Au. The hydrothermal stage is further divided into three substages based on mineral paragenetic relationships. From early to late, they are (1) early substage represented by mineral assemblage of pyrite + arsenopyrite + pyrrhotite + quartz (Q2; Figure 5e,f); (2) intermediate substage with mineral assemblage of electrum + pyrite + chalcopyrite + pyrrhotite + tetradymite (Bi_2Te_2S) + sphalerite + quartz (Q3) + sericite + chlorite (Figures 5i–k and 6); and (3) late substage with mineral assemblage of pyrite + chalcopyrite + galena + sphalerite + siderite + quartz (Q4) + calcite + pyrophyllite (Figure 5k,l). There is evidence indicating white quartz Q2 is crosscut by veinlets of smoky gray quartz (Q3) + sulphides ± chlorite (Figure 5c,d), and veinlets of the hydrothermal stage occasionally cut through mylonitic foliations (Figure 5h). Late veinlets of fine white quartz (Q4) + pyrite + calcite cut across auriferous silicified cataclastic ore (Figure 5l). The hydrothermal stage yields silicified cataclasite and auriferous quartz vein types of ores with electrum, of which the intermediate substage represents the main mineralizing phase. Hydrothermal alteration is represented silicification, pyritization, and sericitization with minor carbonation chloritization and pyrophyllitization. There is a positive correlation of Au mineralization with both silification and pyritization. The supergene stage formed oxidized minerals like malachite, covellite, and limonite.

4 | SAMPLING AND ANALYTICAL METHODS

Samples for fluid inclusion and isotope analyses mainly come from three presently mined deposits, including the Gaocun, Yunxi, and Hehai deposits, and those for $^{40}Ar/^{39}Ar$ dating and LA-ICP-MS U–Pb zircon dating were collected from the Hehai deposit and the Wucun granitic pluton, respectively.

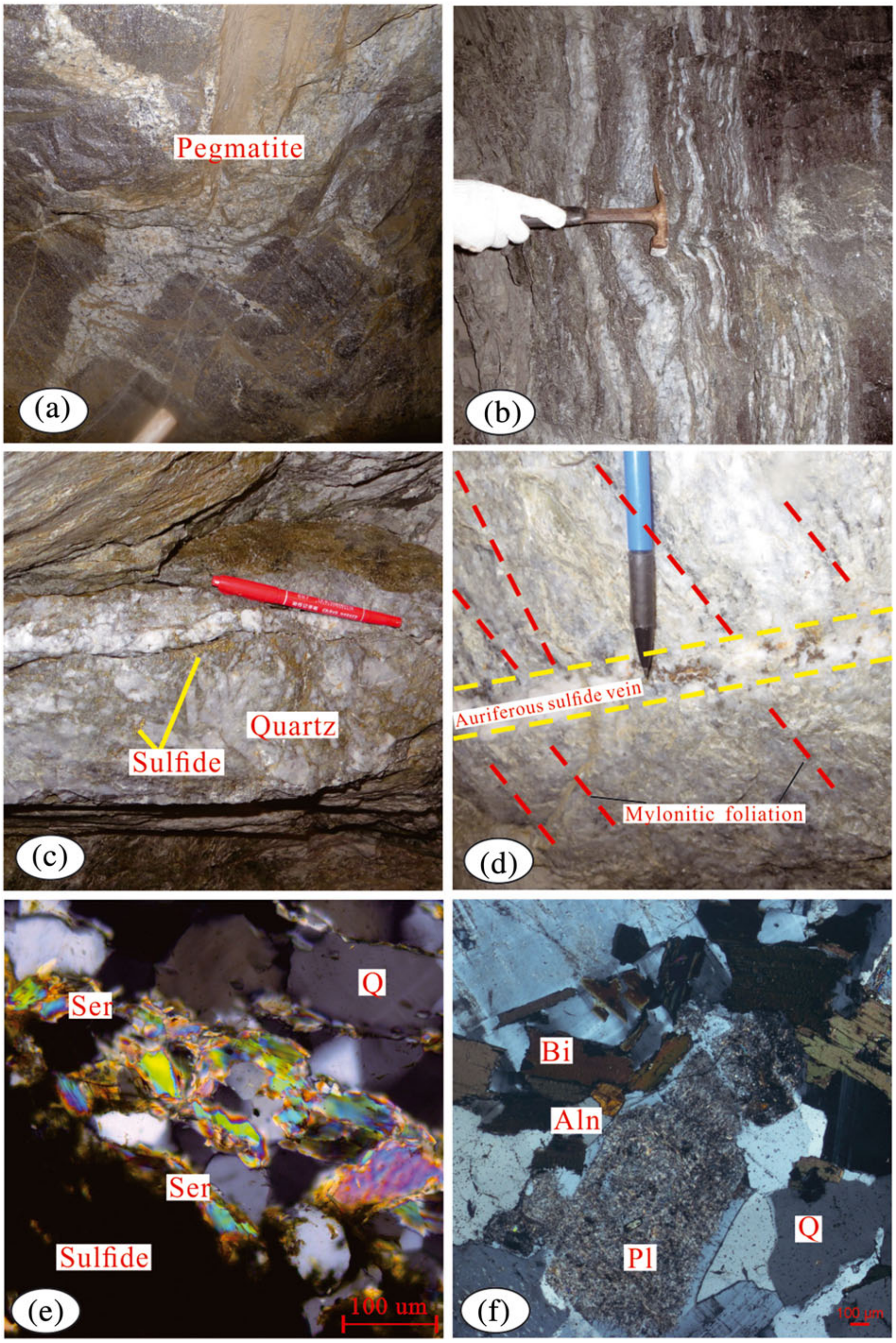

FIGURE 4 Photographs showing host rocks of the Hetai goldfield and microphotographs in cross-polarized light of samples for sericite $^{39}Ar/^{40}Ar$ and zircon U–Pb dating. (a) Migmatite and pegmatite adjacent to mylonite and orebody. (b) Auriferous altered mylonite ore. (c) Auriferous silicified cataclastic ore. (d) Auriferous quartz veins, mica, and sulphides cut across mylonitic foliation. (e) Sample HT104-3 from auriferous quartz veins ore. (f) Sample 17HT05 from Wucun biotite monzonitic granite. Aln: allanite; Bi: biotite; Pl: plagioclase; Q: quartz; and Ser: sericite [Colour figure can be viewed at wileyonlinelibrary.com]

4.1 | Fluid inclusion

Fluid inclusion studies were conducted on tens of ore samples collected from the above mentioned three deposits, including 32 quartz samples for microthermometric analysis, and nine quartz samples for laser Raman spectroscopic analysis. Quartz analysed includes all four types (Q1 to Q4) from all mineralizing stages. Thin sections of ore samples were firstly examined in transmitted light for evaluating occurrence of fluid inclusions before further microthermometry and laser Raman analysis.

Microthermometric measurements of fluid inclusions were conducted using a Linkam TS 600 Heating-Freezing System at the Key Laboratory of Mineralogy and Metallogeny, Chinese Academy of Sciences (KLMMCAS). The precision of temperature measurement

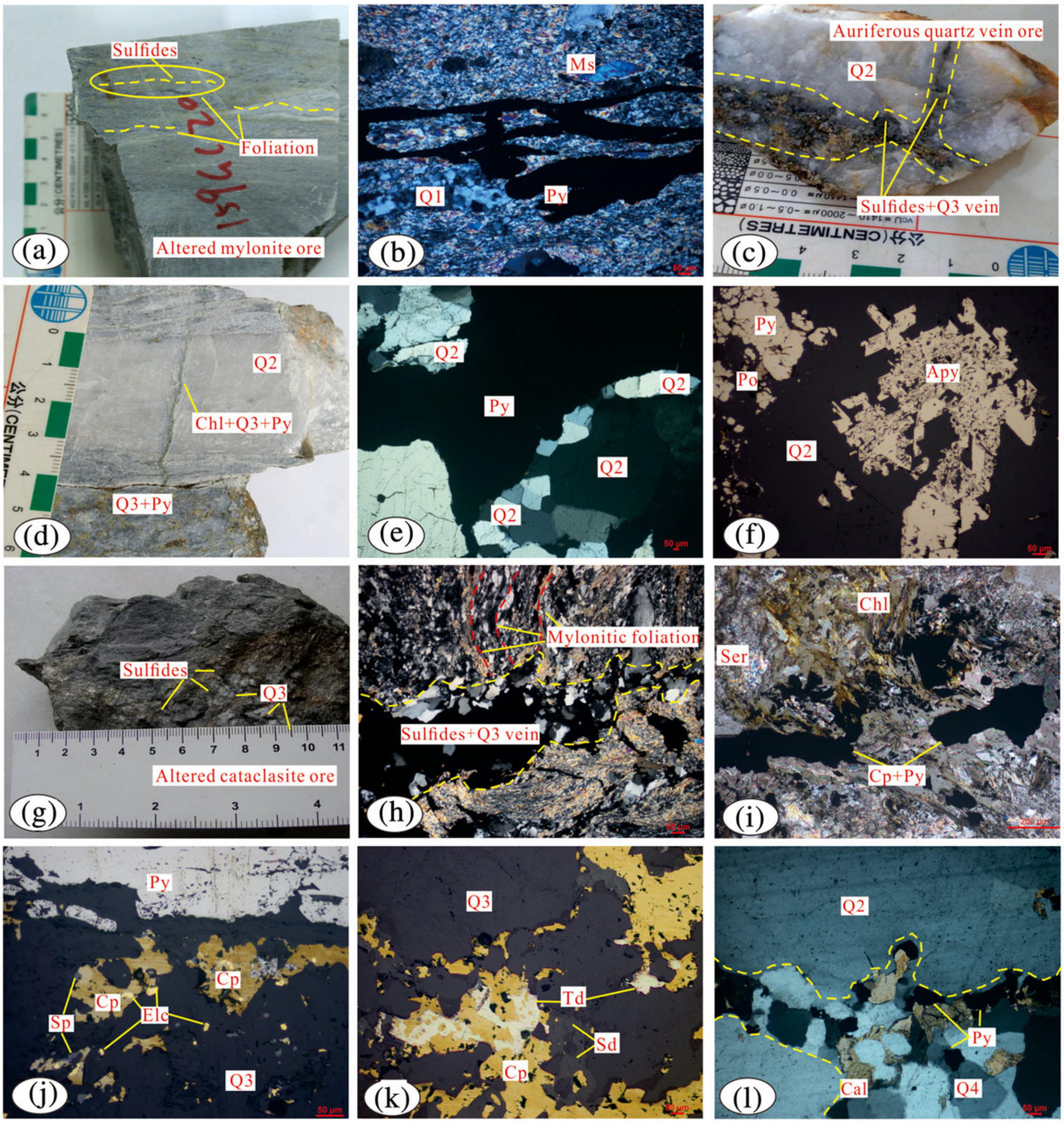

FIGURE 5 Microphotographs and hand specimens showing ore types and mineral assemblages of the Hetai goldfield. (a and b) Auriferous altered mylonite ores containing crumpled and lamellar pyrites and dynamically recrystallized quartz (Q1) parallel or subparallel to mylonitic foliation. (c, d, and e) Auriferous quartz vein ore showing that the later smoky gray quartz (Q3) and sulphide vein cut through the early white quartz (Q2). (f) Quartz + arsenopyrite + pyrite + pyrrhotite of the early substage of hydrothermal mineralization. (g and h) Auriferous silicified cataclastic ores, sulphide intergrowth with quartz that cut across the mylonitic foliation. (i, j, and k) electrum + pyrite + chalcopyrite + pyrrhotite + sphalerite + tetradymite + quartz + chlorite of the intermediate substage of hydrothermal mineralization. (l) pyrite + quartz (Q4) + calcite vein of the late substage of hydrothermal mineralization. (f, j, and k) from reflection light, (b, e, h, i, and l) from cross-polarized light. Abbreviation: Apy: arsenopyrite; Cal: calcite; Cp: chalcopyrite; Elc: electrum; Ms: muscovite; Po: pyrrhotite; Py: pyrite; Q: quartz (Q1–Q4 represent fluid inclusion samples from early to late, respectively); Sd: siderite; Ser: sericite; Sp: sphalerite; and Td: tetradymite [Colour figure can be viewed at wileyonlinelibrary.com]

is ±0.1°C between −100°C and 25°C, ±1°C between 25°C and 400°C, and ±2°C above 400°C. Salinities of the vapour–liquid and solid-bearing inclusions are inferred from ice-melting and halite-melting temperatures respectively, assuming the fluid composition to be of the NaCl–H_2O system (Steele-Macinnis, Lecumberri-Sanchez, & Bodnar, 2012). Salinities of CO_2-bearing fluid inclusions were calculated from clathrate melting temperatures with the help of the MacFlincor software (Brown & Hagemann, 1995).

The volatile compositions of the vapour and liquid phases in fluid inclusions were measured using the Horiba Xplora laser Raman microspectroscopy at the KLMMCAS. An Ar^+ ion laser operating at 44 mW was used to produce an excitation wavelength of 532-nm line. The scanning range of spectra was set between 1,000 and 4,000 cm^{-1} with an accumulation time of 10 s for each scan. The spectral resolution was 0.65 cm^{-1}. The instrument was calibrated with a monocrystalline silicon standard (with a peak of 520.7 cm^{-1}) before the analysis (Jiang et al., 2017).

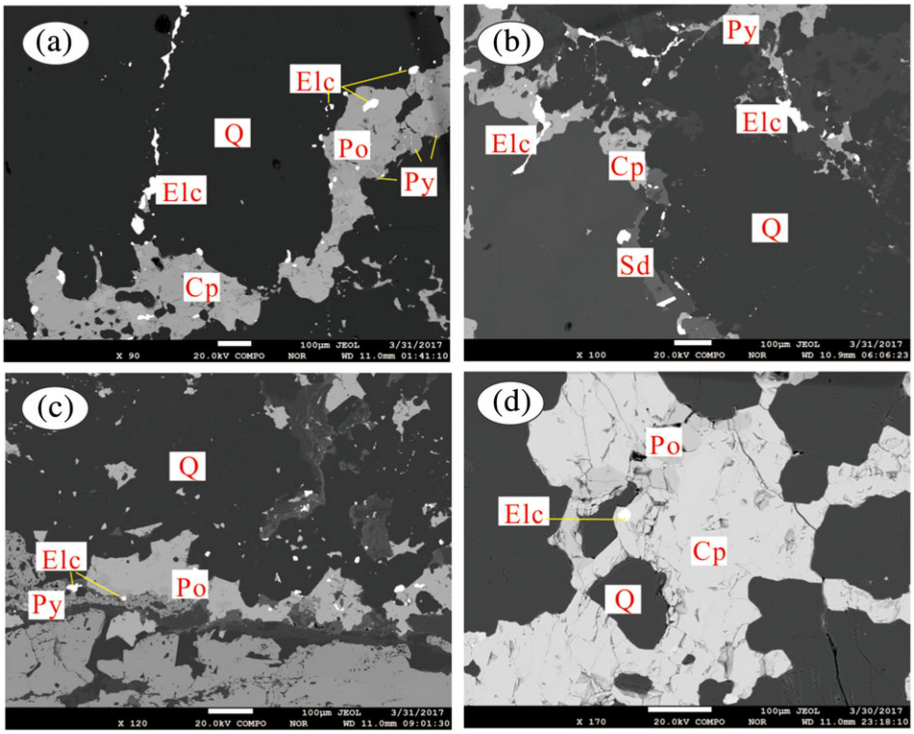

FIGURE 6 Backscattered electron images showing the occurrences and morphologies of gold. (a) Gold stringers in interstices among quartz crystals. (b) Anhedral electrum grains are consistent with pyrite and chalcopyrite. (c) Irregular electrum grains along the boundary between pyrrhotite and pyrite or quartz. (d) Electrum in chalcopyrite as an inclusion. Cp: chalcopyrite; Elc: electrum; Po: pyrrhotite; Py: pyrite; Q: quartz; and Sd: siderite [Colour figure can be viewed at wileyonlinelibrary.com]

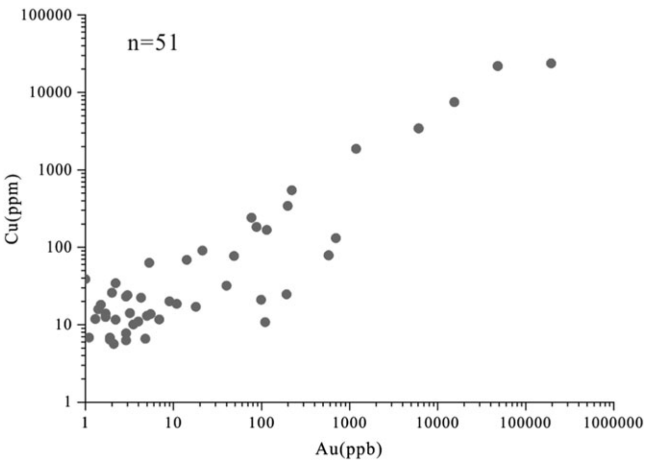

FIGURE 7 Graph of Au vs. Cu concentrations in samples prepared from drill core and mining tunnel collected during the current phase of exploration at Hetai goldfield. Data plotted here show results for 51 bulk rock samples from drill core and mining tunnel collected

4.2 | Isotopes

Stable isotopic analysis is made on single minerals. Fresh ore samples were firstly crushed into fine grains with sizes of 0.1–0.5 mm. After that, individual minerals were handpicked under the binocular microscope and then milled to 75 μm in size.

H–O isotope analyses were carried out on nine single mineral samples, including sericite and chlorite from auriferous silicified cataclastic ores (7) from the Gaocun and Hehai deposits, and pyrophyllite from altered schist (2) of the Yunxi deposit. Of these, sericite and chlorite are from the intermediate substage, while pyrophyllite as a representation mineral of the late substage of the hydrothermal stage. Before measurement, samples were heated in an induction furnace under a vacuum and high temperature (~130°C) condition in order to eliminate the absorbed water in minerals. Oxygen is liberated by reaction with BrF_5 and converted to CO_2 on a platinum-coated carbon rod (Clayton & Mayeda, 1963). Hydrogen is released by reaction with CuO to generate H_2O, which then is reduced to H_2 through the Zn catalyst method (Coleman, Shepherd, Durham, Rouse, & Moore, 1982). The isotope compositions of both gases were analysed on a Finnigan MAT253 mass spectrometer in the Analytical Laboratory, Beijing Research Institute of Uranium Geology, China. All data were normalized with V–SMOW standards with analytical precision better than ±0.2‰ for $\delta^{18}O$ and ±1‰ for δD.

In situ S isotopic analysis is conducted on 28 pyrite grains separated from three samples of auriferous silicified cataclastic ores collected from the Gaocun, Yunxi, and Hehai deposits, respectively. The single pyrite grains were mounted on epoxy chip with 25-mm diameter and carefully polished to expose pyrite sections. The SIMS technique is used with a Cameca IMS1280–HR at the Guangzhou Institute of Geochemistry, Chinese Academy of Sciences (GIGCAS). A primary $^{133}Cs^{+}$ ion beam (~2.0 nA) and a total impact energy of

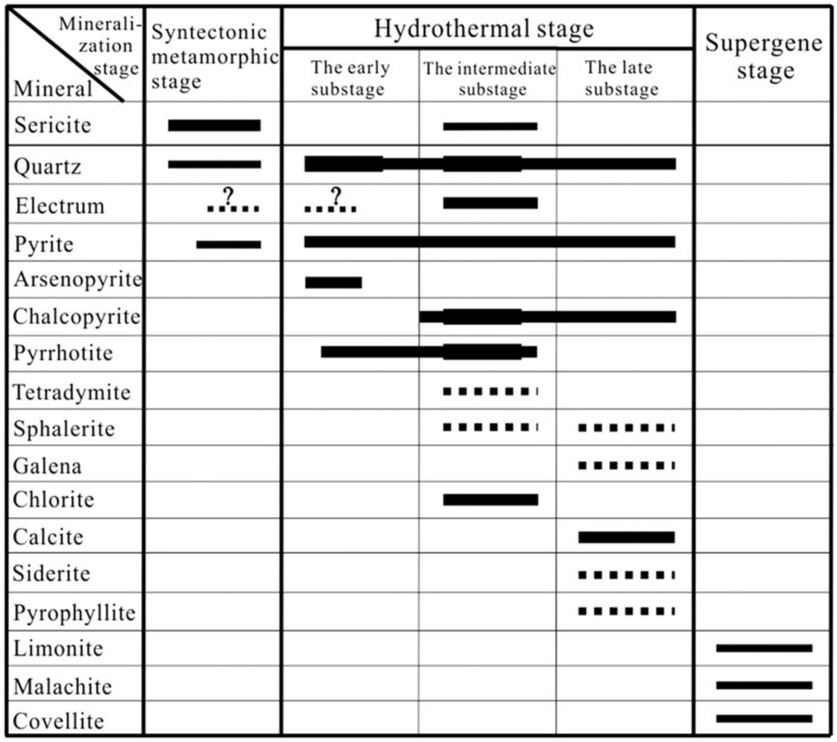

FIGURE 8 Paragenetic sequences for major minerals of the Hetai goldfield. The thickness of the line represents the content of minerals, and dotted lines indicate locally occurring. Question marks represent minerals that are not seen by naked eye

20 keV were used with a spot size of ~15 μm diameter. Twenty-second pre-sputtering was applied to remove the Au coating, and a normal-incidence electron gun is utilized for charge compensation. The mass resolving power was set at ~5,000 to avoid isobaric interference. ^{32}S, ^{33}S, and ^{34}S were collected simultaneously by the multi-collection system. The total analysis time for one spot was about 4 min (R. Li et al., 2017). Data reduction was as outlined in Ushikubo et al. (2014), and the primary standards used in this study were PPP-1 (Gilbert et al., 2014) for pyrite. Py-1 (Molnár et al., 2016) was used as secondary standards in order to monitor the reliability of the whole analytical procedure. A total of 48 spots on 28 pyrites were measured.

Nine samples including schists, migmatites, and granite from Gaocun deposit and Wucun pluton were chosen for Pb isotopic determinations. About 100-mg powder was weighed into a Teflon beaker, spiked and dissolved in concentrated HF at 180°C for 7 hr. Lead was separated and purified by conventional cation-exchange technique (AG1 × 8, 20–400 resin) with diluted HBr as an eluant. Total procedural blanks were less than 50 pg Pb. Isotopic ratios were measured by a VG-354 mass-spectrometer at the GIGCAS. Repeated analyses of SRM 981 yielded average values of $^{206}Pb/^{204}Pb$ = 16.9 ± 4 (2σ), $^{207}Pb/^{204}Pb$ = 15.498 ± 4 (2σ) and $^{208}Pb/^{204}Pb$ = 36.728 ± 9 (2σ). External precisions are estimated to be less than 0.005 and 0.0015. The analytical procedure is similar to that described by Zhu et al. (2001).

4.3 | Geochronology

4.3.1 | $^{40}Ar/^{39}Ar$ dating

Radiometric dating is conducted on sericite (sample 14HT104-3) from auriferous cataclastic ores of the Hehai deposit (Figure 4e). Samples were firstly crushed into 0.25–0.425 mm, and then single mineral separates were handpicked under binocular. The packaged 200 mg samples were irradiated in the Swimming Pool reactor at Sichuan, along with Chinese Standard ZBH-25 (Biotite, 132.7 Ma) as a flux monitor. The irradiation time was 48 hr, the integral neutron flux was 9×10^{12} n/cm^2 s and the irradiation parameter J was 0.0123. The argon isotope ratios were analysed using a GVI-5400 noble gas mass spectrometer in the GIGCAS. The mass spectrometer is equipped with a high Faraday and an electron multiplier. The Faraday feedback resistor is 10^{11} Ω. The source trap current is set at 200 μA during measurement. The signal intensity ratio of the multiplier to the Faraday is about 0.84. The $^{40}Ar/^{39}Ar$ results were calculated and plotted using the software ArArCALC (version 2.52; Koppers, 2002). Correction factors for interfering argon isotopes derived from irradiated CaF_2 and K_2SO_4 are $(^{39}Ar/^{37}Ar)_{Ca} = 8.984 \times 10^{-4}$, $(^{36}Ar/^{37}Ar)_{Ca} = 2.673 \times 10^{-4}$, and $(^{40}Ar/^{39}Ar)_K = 5.97 \times 10^{-3}$ (Bai, Wang, Jiang, & Qiu, 2013). The data were corrected for system blanks, mass discrimination, and interfering neutron reactions with Ca and K, and analytical precision was estimated at ±1 σ.

4.3.2 | LA-ICP-MS U–Pb zircon dating

Zircon grains were separated from the Wucun biotite monzonitic granite samples (17HT05, Figure 4f) using conventional heavy liquid and magnetic separation techniques. Representative zircon grains were handpicked under a binocular microscope and mounted in an epoxy resin disk, which was then polished. Transmitted and reflected light micrographs and CL (cathodoluminescence) images were taken on the zircons to reveal their internal structures. LA-ICP-MS U–Pb dating on zircons was conducted at the GIGCAS. The analytical procedures are the same as described by C. Y. Li et al. (2012). Off-line selection and integration of background and analytic signals, and time drift correction and quantitative calibration for U–Pb dating, were performed using ICPMSDataCal (Y. S. Liu et al., 2008). Concordia diagram was processed using Isoplot (Ludwig, 2003).

5 | RESULTS

5.1 | Fluid inclusion study

5.1.1 | Petrography of fluid inclusions

Based on morphologies and different phase states at room temperature, fluid inclusions can be categorized primarily as four types: aqueous (type 1), aqueous-carbonic (type 2), CO_2-rich (type 3), and solid-bearing three-phase fluid inclusions (type 4).

Aqueous inclusions (type 1) contain only vapour (V) and liquid (L) phases. This type of inclusions commonly shows irregular shapes with sizes varying from 3 to 15 μm. The vapour bubbles are generally bright and colourless and have diameters ranging from 1 to 3 μm (Figure 9a–c).

Aqueous-carbonic inclusions (type 2) are dominated by water but also have a relatively low contents of CO_2 (10–30 vol.%). This type of inclusions is transparent and has elliptical or elongate shape with long dimension of 2–10 μm (Figure 9d,e). Most of them show two phases (liquid H_2O and CO_2-rich vapour) at room temperature and upon heating the fluid inclusions are homogenized into a single liquid phase. During cooling, some (Type 2a) keep the two-phase state while others (Type 2b) display three phases (VCO_2, LCO_2, and LH_2O).

CO_2-rich inclusions (type 3) consist of a dominant CO_2 phase and a minor aqueous phase at room temperature and are approximated by the CO_2–H_2O system (Diamond, 2001). Morphology is generally round or oval and the sizes are between 5 and 20 μm. The gas bubbles are commonly dark and brown and occupy 60- to 90-vol.% CO_2 of the inclusions (Figure 9f). This type of inclusions comprises two phases (liquid H_2O and CO_2-rich gas) at room temperature and three phases (VCO_2–LCO_2–LH_2O) during cooling. During heating, inclusions can be fully homogenized into the carbonic phase, rather than the aqueous phase as for the type 2 inclusions.

Solid-bearing three-phase inclusions (type 4) contain vapour, liquid water, and solid mineral at room temperature. They exhibit irregular elongate shapes with long dimension of 4 to 10 μm. The solid minerals comprise pale dark, translucent halite with cubic shape (Figure 9g).

These different types of fluid inclusions have specific distribution in quartz grains formed at different stages of mineralization. The earliest banded quartz (Q1) of the syntectonic metamorphic stage contains only type 1 fluid inclusions (Figure 9a,b). The early substage quartz (Q2) of hydrothermal mineralization contains types 2 and 4 inclusions, of which type 2 mainly occurs in clusters and type 4 in isolation (Figure 9d,e,g). The intermediate substage quartz (Q3) of hydrothermal mineralization comprises types 2a and 3 fluid inclusions. Type 2a and 3 inclusions sometimes coexist within a single microdomain (Figure 9h,i). On the contrary, the late substage quartz (Q4) of hydrothermal mineralization contains only the type 1 fluid inclusions (Figure 9c).

A scheme of generations can be recognized from grouping patterns of inclusions. One category of inclusions is lined along linear microcracks across several quartz grains (Figure 9j). This pattern of inclusions is dominant in number and might have been trapped after Au mineralization. Subordinate inclusions are randomly clustered in certain domains within individual quartz grains (Figure 9c,e). The kind of inclusions is considered to be captured during growth of quartz grains and is coeval with Au mineralization (Figure 9h,i). In addition, there are few inclusions developed in healed fractures (Figure 9b) or growth zones (Figure 9k) within single quartz grains. They might have also formed during growth of quartz grains corresponding to a single phase or multiple phases and thus are associated with different substages of Au mineralization. The following experimental data mainly come from those fluid inclusions interpreted to be entrapped during growth of quartz grains.

5.1.2 | Microthermometry

Results of temperature and salinity measurement are listed in Table 1 and plotted in Figures 10 and 11. The microthermometric data of the various types of fluid inclusions from different stages of mineralization are described in detail as follows.

1. Syntectonic metamorphic stage of mineralization. Only type 1 inclusions in this stage of quartz reach homogenization upon disappearance of vapour phase. The corresponding homogenization temperatures range from 350°C to 400°C. The ice-melting temperatures (Tim) range from −3.5 to −2°C, which correspond to salinities from 5.7- to 3.4-wt.% NaCl equiv.
2. Early substage of hydrothermal mineralization. Two types of inclusions (types 2 and 4) are identified in this substage of quartz, of which type 2 can be divided into two subtypes 2a and 2b. The type 2a has first melting temperatures ranging from −25.1°C to −14°C with most of them clustered around −20.8°C suggesting a dominant $NaCl$–H_2O system. The ice-melting temperatures range from −9°C to −0.8°C, corresponding to salinities of 12.9- to 1.4-wt.% NaCl equiv. Homogenization temperatures span the interval from 160°C to 345°C with two peaks between 250°C and 320°C, and 180°C and 220°C, respectively. Here, we choose the former temperature group as mineralization temperature, which is congruent with a temperature range of ca. 290°C to 350°C estimated from arsenopyrite thermometry for the same stage (Jiao, Deng, et al., 2017). For the type 2b fluid inclusions, the measured first melting temperatures of solid CO_2 vary from −79.2°C to −56.6°C with most of them slightly lower than the triple point for pure CO_2 (−56.6°C), suggesting the presence of minor other components such as CH_4 as indicated by laser Raman spectroscopy analyses. The melting of CO_2 clathrate occurs at temperatures between 5.8°C and 7.5°C, thus corresponding to salinities in the range of 7.7- to 4.8-wt.% NaCl equiv. Temperatures at which gas CO_2 is homogenized to liquid vary considerably from 14°C to 20.5°C

and temperatures at which the two phases are totally homogenized to aqueous phase range from 268°C to 282°C. For type 4 fluid inclusions, upon heating, the dissolution of the halite crystal generally occurs at temperatures between 275°C and 285°C, but total homogenization indicated by vapour disappearance occurs between 325°C and 345°C. Salinities determined from the

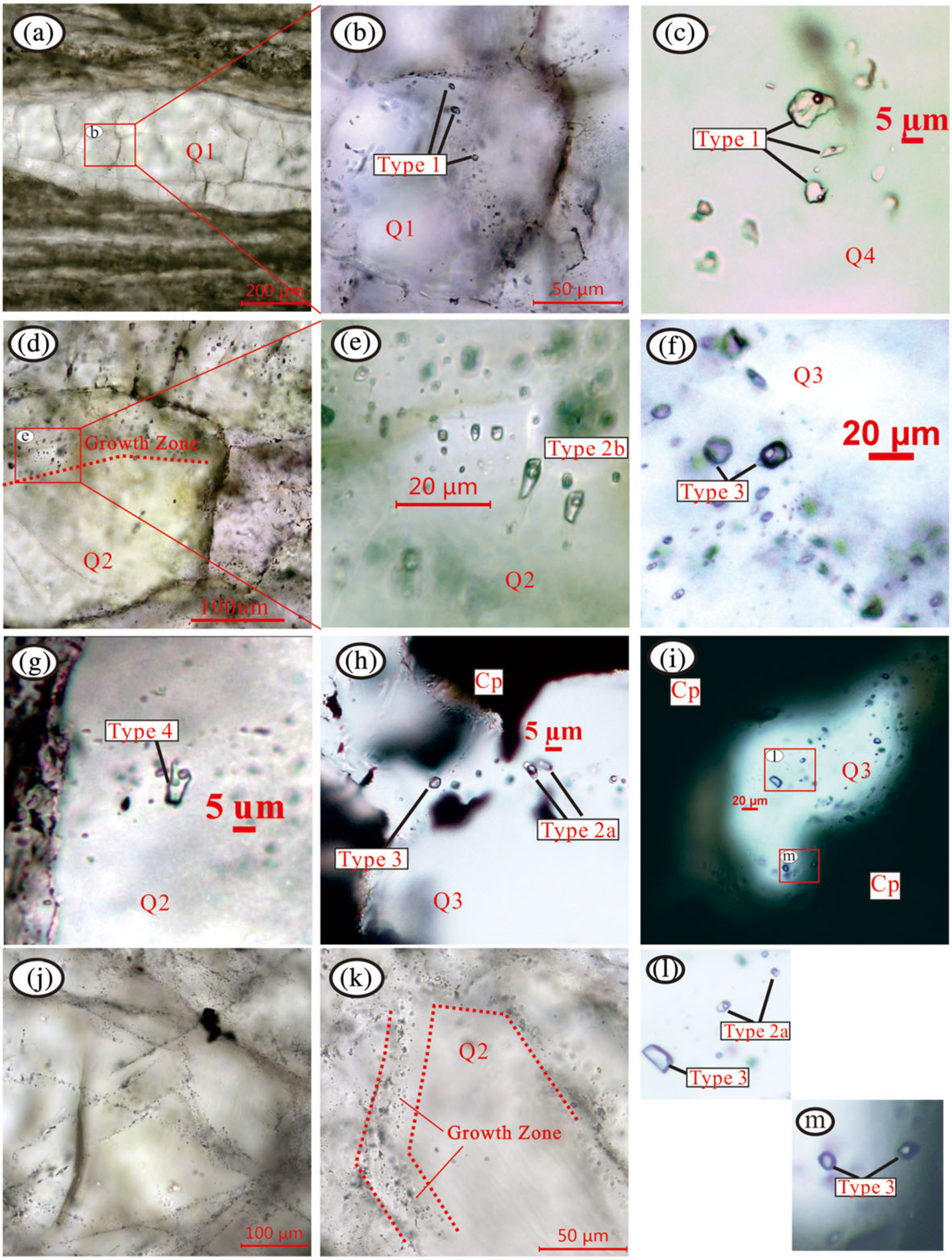

FIGURE 9 Photomicrographs of fluid inclusions in quartzs from the Hetai ores. (a, b, and c) Aqueous fluid inclusions (type 1) in Q1 (a and b) and Q4 (c); (d and e) type 2b fluid inclusion in Q2. (f) Type 3 fluid inclusion in Q3. (g) Type 4 fluid inclusion in Q2. (h and i) Coexisting type 2a and type 3 fluid inclusion in Q3. (j) Secondary fluid inclusions. (k) Type 2 fluid inclusions in growth zones in Q2. Abbreviation: type 1: aqueous inclusions; type 2: CO_2-bearing aqueous inclusions (type 2a keep the two-phase state while type 2b is slight rich in CO_2 display three phases [VCO_2, LCO_2, and LH_2O] during cooling); type 3: CO_2-rich inclusions; type 4: solid-bearing inclusions; Cp: chalcopyrite [Colour figure can be viewed at wileyonlinelibrary.com]

TABLE 1 Microthermometric data of fluid inclusions in the Hetai goldfield

Stage	Sample	Type	Number	Tfm	Tim	Tcm	$ThCO_2$	Th	Salinity (wt.% NaCl)
Mylonitic stage	Q1	1	7	−20 to −19	−2 to −3.5			350–400 (L) 275–285 (*)	3.4–5.7
Early hydrothermal substage	Q2	4 2a 2b	2 136 7	 −25.1 to −14 −79.2 to −56.6	−9 to −0.8	5.8–7.5	14–20.5	325–345 (L) 160–345 (L) 268–282 (L)	36.3–37.1 1.4–12.9 4.8–7.7
Intermediate hydrothermal substage	Q3	2a 3	61 8	−20 to −15.7 −58.2 to −56	−7.8 to −0.3	7.5–9.4	−14-17	138–245 (L) 197–214 (C)	0.5–11.5 1.2–4.8
Late hydrothermal substage	Q4	1	29	−22 to −16.3	−4.6 to −0.1			110–207(L)	0.2–7.3

Note. Tfm (°C) = first melting temperature; Tim (°C) = ice-melting temperatures; Tcm (°C) = melting temperature of CO_2–H_2O clathrate; $ThCO_2$ (°C) = partial homogenization temperature of CO_2; Th (°C) = final homogenization temperature; L and C represent liquid and carbonic phases after homogenization of fluid inclusions, respectively.

*Referring to halite-dissolution temperature.

dissolution temperatures of halite vary from 36.3- to 37.1-wt.% NaCl equiv. Only two inclusions with such high salinity values were discovered, and they were likely generated by accidental entrapment and thus cannot represent compositions of parental fluids. Consequently, they will not be further discussed below.

3. Intermediate substage of hydrothermal mineralization. Quartz from this substage (Q3) contains types 2a and 3 inclusions. Among these, the type 2a inclusions have ice-melting temperatures ranging from −7.8°C to −0.3°C corresponding to salinities from 11.5- to 0.5-wt.% NaCl equiv. Homogenization temperatures vary from 138°C to 245°C with a peak between 150°C and 210°C. The type 3 inclusions (Figure 9f) have first melting temperatures varying from −58.2°C to −56°C and are homogenized to liquid phase at temperatures from −14°C to 17°C and to carbonic phase from 197°C to 214°C. However, for those inclusions consisting of nearly pure CO_2, the final homogenization temperatures were barely observed. The melting of CO_2 clathrate occurred at temperatures between 7.5°C and 9.4°C, reflecting salinities in the range of 4.8- to 1.2-wt.% NaCl equiv. consistent with the type 2a fluid inclusions in the same microdomain.
4. Late substage of hydrothermal mineralization contains only the type 1 fluid inclusions in quartz (Q4). First melting temperatures of fluid inclusions in quartz range from −22°C to −16.3°C, indicating dominance of the NaCl–H_2O system. The ice-melting temperatures span from −4.6°C to −0.1°C, corresponding to salinities of 7.3- to 0.2-wt.% NaCl equiv. These inclusions homogenized to a single liquid phase at temperatures from 110°C to 207°C, and most are clustered between 140°C and 166°C.

5.1.3 | Laser Raman spectroscopy

Laser Raman spectra for the vapour phase of type 2 fluid inclusions of the early substage of hydrothermal mineralization show peaks of CO_2 (1,285 and 1,389 cm^{-1}) and CH_4 (2,918 cm^{-1}; Figure 12a). This result is consistent with the microthermometric observations (Table 1). In contrast, the liquid phase only has a peak of H_2O (3,310–3,610 cm^{-1}; Figure 12a). Likewise, the spectra of gas phase for type 3 fluid inclusions of the intermediate substage of hydrothermal mineralization also shows peaks of CO_2 and CH_4 (Figure 12b) in contrast with a single water peak in the liquid phase. However, both the liquid and vapour phases in the inclusions of the late substage of hydrothermal mineralization are almost pure H_2O (3,310–3,610 cm^{-1}; Figure 12c).

5.2 | H–O isotopes

The H and O isotopic compositions of the single minerals are listed in Table 2 and illustrated in Figure 13. The $\delta^{18}O_{H_2O}$ values refer to O isotope of hydrothermal fluids coexisting with those minerals and are calculated from different mineral-water systems (L. G. Zhang, 1989; Y. F. Zheng, 1993, 1998). Because of the low fractionation factor of hydrogen isotopes between minerals and water at low temperatures (<330°C), the δD values of minerals were regarded as representing those of mineralizing fluids (Zhao & Zheng, 2000; Y. F. Zheng & Chen, 2000). The temperatures used in calculation are the peak values of fluid inclusion homogenization temperatures for intermediate (518.5 K) and late (480.5 K) substages, which is also consistent with the temperature from mineral geothermometers (Jiao, Deng, et al., 2017). The calculated $\delta^{18}O_{H_2O}$ values of fluids coexisting with altered minerals of auriferous cataclastic ore (intermediate substage) range from 5.47‰ to 7.46‰ with a mean value of 6.73‰. The δD values of these altered minerals vary from −98.1‰ to −62.4‰ with a mean value of −77.3‰. The calculated $\delta^{18}O_{H_2O}$ and δD values of fluids coexisting with pyrophyllites from late substage of hydrothermal mineralization stage are from −1.13‰ to 2.07‰ and from −56.0‰ to −54.0‰, respectively.

5.3 | S–Pb isotopes

Table 3 lists 48 $\delta^{34}S_{CDT}$ data of pyrites from auriferous silicified cataclastic ores formed in the main stage (i.e., early and intermediate substages) of hydrothermal mineralization. The $\delta^{34}S_{CDT}$ values range from −1.5‰ to −5.2‰ with an average of −3.4‰, which

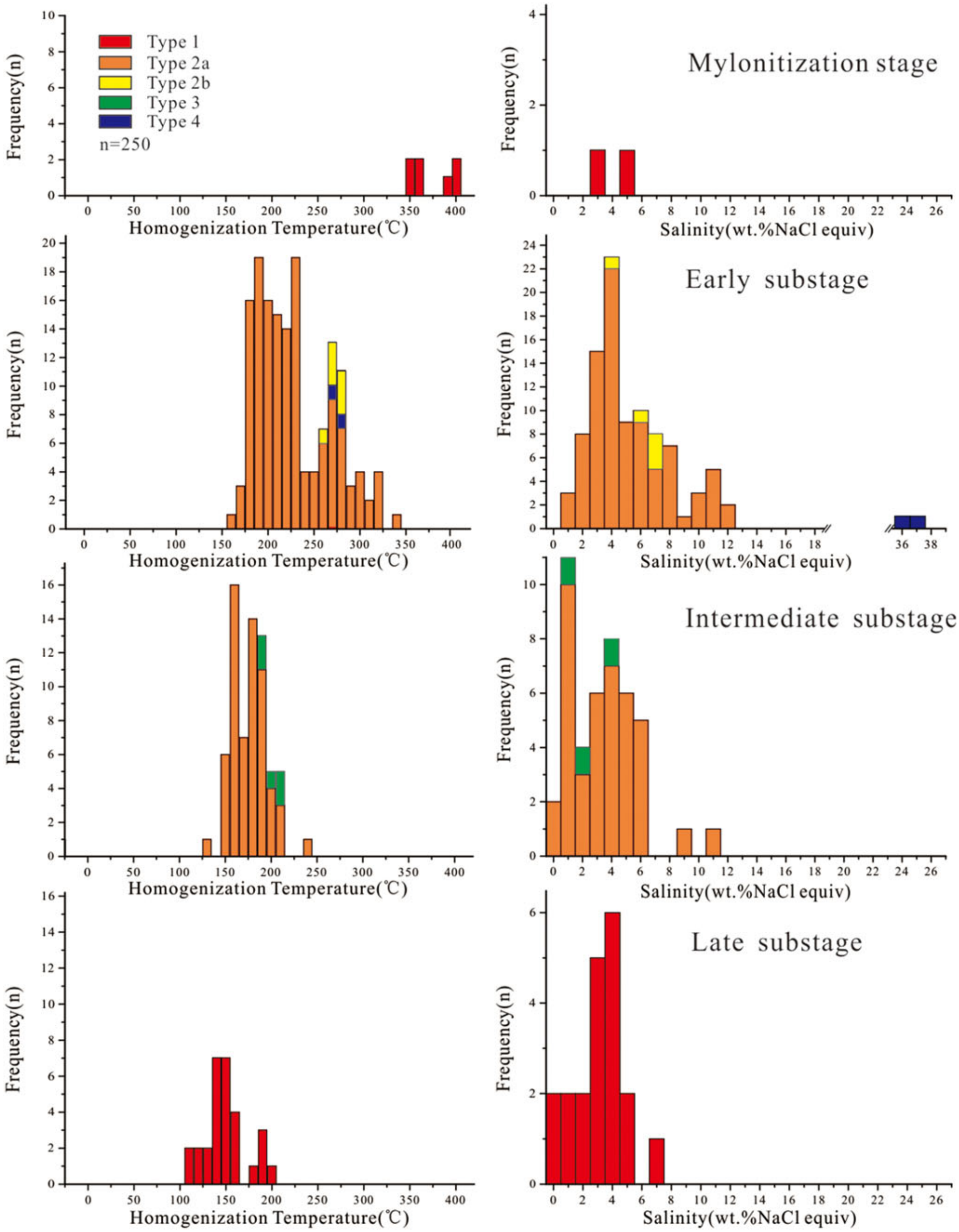

FIGURE 10 Histograms of both the homogenization temperatures and salinities of fluid inclusions, note from top to bottom, representing the syntectonic metamorphic stage of mineralization and the early, intermediate, and late substages of hydrothermal mineralization, respectively [Colour figure can be viewed at wileyonlinelibrary.com]

shows a pronounced normal distribution (Figure 14). Moreover, our results are consistent with previously published $\delta^{34}S_{CDT}$ values of sulphides from various ores by traditional method (Fu, 1988; Jiao, Wang, et al., 2017; Lu et al., 1990; Lu, 1993).

The analytical results of lead isotopes of nine samples are presented in Table 4. Overall, the isotopic ratios of whole-rocks fall in small ranges individually. Schist has $^{206}Pb/^{204}Pb$ ratios ranging from 19.400 to 19.726, $^{207}Pb/^{204}Pb$ from 15.840 to 15.940, and $^{208}Pb/^{204}Pb$ from 38.320 to 40.773. The migmatite samples yield $^{206}Pb/^{204}Pb$ values of 13.712–18.394, $^{207}Pb/^{204}Pb$ values of 15.474–15.753, and $^{208}Pb/^{204}Pb$ values of 38.583–38.995. The granite samples yield $^{206}Pb/^{204}Pb$ values of 17.665–19.118, $^{207}Pb/^{204}Pb$ values of 15.580–15.782, and $^{208}Pb/^{204}Pb$ values of 38.607–39.146. By contrast, Pb isotopic compositions of gold-bearing sulphides are similar to those of the Wucun granites rather than the schist and migmatite. Most of the lead isotope data plot above or adjacent to the orogen and upper crust lines on the $^{207}Pb/^{204}Pb$ versus $^{206}Pb/^{204}Pb$ and $^{208}Pb/^{204}Pb$ versus $^{206}Pb/^{204}Pb$ diagrams (Figure 15).

5.4 | Geochronology

The $^{40}Ar/^{39}Ar$ age data are presented in Table 5, and the age spectra and corresponding isochron are shown in Figure 16. The sericite

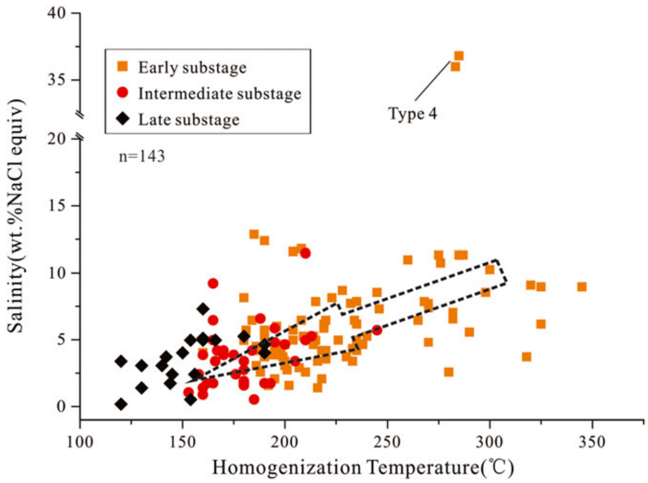

FIGURE 11 Homogenization temperatures versus salinities of fluid inclusions. Abbreviation: type 4: solid-bearing inclusions, the rest of the data are from aqueous, CO_2-bearing aqueous and CO_2-rich inclusions [Colour figure can be viewed at wileyonlinelibrary.com]

sample 14HT104-3 from the auriferous cataclastic ore of the Hehai deposit yielded a relatively flat age spectrum and the eighth to fifteenth heating steps constitute a well-defined plateau giving an age of 159.3 ± 0.8 Ma (Figure 16a). The plateau age is consistent in error limit with corresponding isochron age is 159.1 ± 0.8 Ma (Figure 16b).

The U–Pb isotope data are tabulated in Table 6 and graphically illustrated in the concordia diagram (Figure 16c,d). The U–Pb ages are cited as 1σ errors at the 95% confidence level. Zircons from the biotite monzonitic granite are generally euhedral (size: 100–300 μm; length/width ratio: 2:1–3:1). Most zircons are light yellow in colour and transparent to translucent and prismatic, and exhibit clear oscillatory zoning in CL images (Figure 16d). Twenty analyses have yielded Th = 52–1,102 ppm, U = 115–6,526 ppm and Th/U = 0.04–2.76, with the latter suggesting an igneous origin for the zircons (Y. B. Wu & Zheng, 2004). Three of the $^{206}Pb/^{238}U$ ages were 832 ± 7, 512 ± 4, and 210 ± 2 Ma, and the others ranged from 151 ± 2 to 161 ± 2 Ma (Figure 16c). We consider the three former ages to be inherited from the magma source or xenocrysts captured from country rocks. Thirteen analyses on thirteen grains yield concordant or nearly concordant (Concorde degrees >93%) ages with a lower intersection $^{206}Pb/^{238}U$ age of 158.1 ± 1.9 Ma (MSWD = 1.11, *n* = 13; Table 6; Figure 16d), interpreted as the crystallization age of the Wucun biotite monzonitic granite.

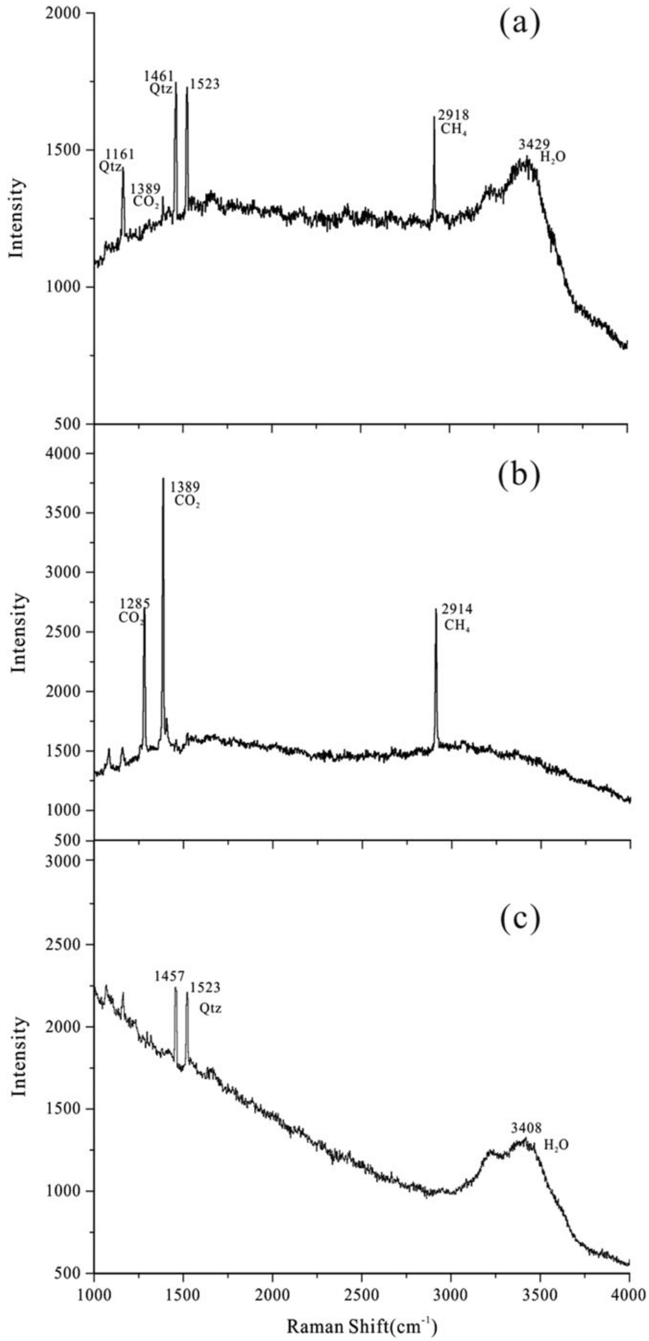

FIGURE 12 Representative Raman spectra of fluid inclusions of the Hetai goldfield, note from top to bottom, representing the early, intermediate, and late substages of hydrothermal mineralization, respectively

6 | DISCUSSION

6.1 | Timing of the mineralization

The analysed hydrothermal sericite is clearly related to or has close petrographic relationships with gold mineralization in this study (Figure 4e). Thus, $^{40}Ar/^{39}Ar$ dating of these hydrothermal minerals provides direct constraints on the timing of gold mineralization. Here, a 159.3 ± 0.8 Ma sericite $^{40}Ar/^{39}Ar$ age of auriferous cataclastic ore from the Hehai deposit was obtained. The $^{40}Ar/^{39}Ar$ age represents the time when the sericite sample cooled below the closure temperature of argon isotopes in mica. Because the temperatures of gold deposition, as indicated by the final homogenization temperatures of types 2a and 3 fluid inclusions in Q3 (ca. 197°C to 214°C; Table 1) and chlorite thermometry (ca. 230°C to 260°C) from the hydrothermal intermediate substage (Jiao, Deng, et al., 2017), are lower than the argon closure temperature in mica (300°C–350°C; McDougall & Harrison, 1999), the present $^{40}Ar/^{39}Ar$ age can also be reliably

TABLE 2 δD and $\delta^{18}O$ values of hydrothermal alteration in the Hetai goldfield (‰)

Stage	Sample	$\delta D_{V\text{-}SMOW\ mineral}$ (‰)	$\delta O_{V\text{-}SMOW\ mineral}$ (‰)	$\delta D_{V\text{-}SMOW\ water}$ (‰)	$\delta O_{V\text{-}SMOW\ water}$ (‰)	Data source
Intermediate substage	Sericite	−98.10	8.80	−98.10	5.98	This study
Intermediate substage	Sericite	−68.90	9.90	−68.90	7.08	
Intermediate substage	Sericite	−78.50	10.20	−78.50	7.38	
Intermediate substage	Sericite	−74.40	9.20	−74.40	6.38	
Intermediate substage	Sericite	−75.40	10.20	−75.40	7.38	
Intermediate substage	Sericite	−83.60	8.30	−83.60	5.48	
Intermediate substage	Chlorite	−62.40	9.70	−62.40	7.47	
Late substage	Pyrophyllite	−56.00	8.10	−56.00	−1.13	
Late substage	Pyrophyllite	−54.00	11.30	−54.00	2.07	
Late substage	Calcite*		−1.91		0.21	Lu, 1993
Late substage	Calcite*		−2.22		0.39	
Late substage	Calcite*		−3.53		−0.51	
Unknown	Quartz		11.00	−84.00	5.96	H. N. Wang et al., 1989
Unknown	Quartz		14.50	−56.90	7.6	
Unknown	Quartz		11.50	−59.50	2.5	
Unknown	Quartz		8.60	−54.00	−0.4	
Unknown	Quartz		7.00	−81.50	−1.96	
Unknown	Quartz			−57	5.71	
Unknown	Quartz			−60	0.21	
Unknown	Quartz			−54	−2.69	
Unknown	Quartz			−82	−4.28	
Unknown	Quartz		11	−84	5.96	Lu, Wang, Shen, & Dai, 1990
Unknown	Quartz		14.5	−56.9	7.6	
Unknown	Quartz		11.5	−59.5	2.5	
Unknown	Quartz		8.6	−54	−0.4	
Unknown	Quartz		7	−81.5	−1.96	
Unknown	Quartz		13.71	−90.7	4.65	Tu & Gao, 1991
Unknown	Quartz		14.14	−93.7	5.08	
Unknown	Quartz		12.91	−77.2	3.85	
Unknown	Quartz		13.7	−83.8	4.64	
Unknown	Quartz		13.13	−81.7	4.07	
Unknown	Quartz		13.87	−91.4	4.81	
Unknown	Quartz		15.37	−82.6	6.31	
Unknown	Quartz		12.95	−74.8	3.89	
Unknown	Quartz		12.28	−81.5	3.22	
Unknown	Quartz			−70.3	−3.7	W. Liu et al., 2005
Unknown	Quartz			−61.7	−5.05	
Unknown	Quartz			−70.8	−3.91	
Unknown	Quartz			−92.4	0.35	
Unknown	Quartz			−90.4	−1.55	
Unknown	Quartz	−71.4	10.8	−71.4	1.9	Jiao, Wang, et al., 2017
Unknown	Quartz	−66	11.7	−66	2.8	
Unknown	Quartz	−74.3	10.8	−74.3	1.9	
Unknown	Quartz	−59.5	10	−59.5	1.1	
Unknown	Quartz	−74.5	11.8	−74.5	2.9	
Unknown	Quartz	−59.4	12	−59.4	3.1	
Unknown	Quartz	−63.1	12	−63.1	3.1	
Unknown	Quartz	−61.1	10.8	−61.1	1.9	
Unknown	Quartz	−61.1	12.6	−61.1	0.42	
Unknown	Quartz	−52.4	13.5	−52.4	1.32	

(Continues)

TABLE 2 (Continued)

Stage	Sample	$\delta D_{V\text{-}SMOW\ mineral}$ (‰)	$\delta O_{V\text{-}SMOW\ mineral}$ (‰)	$\delta D_{V\text{-}SMOW\ water}$ (‰)	$\delta O_{V\text{-}SMOW\ water}$ (‰)	Data source
Unknown	Quartz	−58.3	12.5	−58.3	0.38	
Unknown	Quartz	−62	11.4	−62	−0.66	
Unknown	Quartz	−67.6	12.7	−67.6	0.71	
Unknown	Quartz	−62.2	19.9	−62.2	7.97	
Unknown	Quartz	−83.1	19.1	−83.1	7.23	
Unknown	Quartz	−64.9	16.4	−64.9	4.59	
Unknown	Quartz	−72.8	17.9	−72.8	7.86	

Note: The $\delta^{18}O_{H_2O}$ values were calculated according to $1{,}000\ln\alpha_{muscovite\text{-}water} = 4.10 \times 10^6/T^2 - 7.61 \times 10^3/T + 2.25$, $1000\ln\alpha_{pyrophyllite\text{-}water} = 4.40 \times 10^6/T^2 - 5.62 \times 10^3/T + 1.87$, $1{,}000\ln\alpha_{chlorite\text{-}water} = 3.97 \times 10^6/T^2 - 8.19 \times 10^3/T + 2.36$ (Y. F. Zheng, 1993, 1998) and $1{,}000\ln\alpha_{calcite\text{-}water} = 2.78 \times 10^6/T^2 - 2.89$ (L. G. Zhang, 1989).

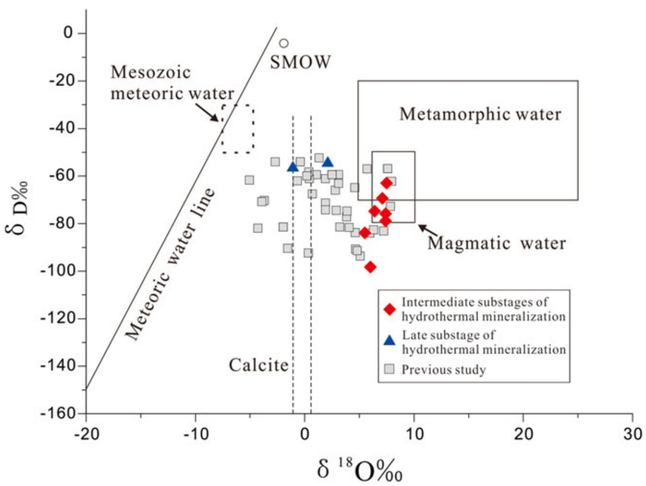

FIGURE 13 δD and $\delta^{18}O$ characteristics of the ore-forming fluids of the Hetai goldfield. Mesozoic meteoric water field is from L. G. Zhang (1989), the range of dotted line present fluid $\delta^{18}O$ values calculated from O isotopes of calcites. Previous data are from Jiao, Wang, et al. (2017); W. Liu et al. (2005); Lu (1993); Tu and Gao (1991); and H. N. Wang et al. (1989) [Colour figure can be viewed at wileyonlinelibrary.com]

interpreted as the timing of hydrothermal alteration and gold deposition for the Hetai goldfield. This new age is roughly in accordance with previously reported 152.5 ± 3.1 Ma of hydrothermal zircons U–Pb age (Zhai et al., 2006) and 157.1 ± 1.0 Ma of sericite $^{40}Ar/^{39}Ar$ age (C. Wang, Zhang, et al., 2012) of ore-bearing rocks from the same deposit, which suggests that the Hetai goldfield formed during the Late Jurassic. However, these ages are significantly younger than 492 ± 16 Ma of SHRIMP zircon U–Pb age (Zhai et al., 2005) and 175.5 ± 4.3 Ma of pyrrhotite Re–Os isochron age from auriferous quartz veins (C. Wang, Zhang, et al., 2012). The zircon grains that gave the old age may be derived from the wall rock (migmatite: 490 ± 62 Ma; G. Y. Wu, 1986), whereas the pyrrhotite that produced the old Re–Os isochron age may have been formed in an event unrelated to gold mineralization based on the description of the samples provided in C. Wang, Zhang, et al. (2012). On the other hand, all the Late Jurassic ages are roughly coeval within error with zircon U–Pb ages of the Wucun pluton near the goldfield, including a zircon U–Pb age of 153.6 ± 2.1 Ma by isotopic dilution method (Zhai et al., 2005) and a LA-ICP-MS zircon U–Pb age of 158.1 ± 1.9 Ma for the biotite monzonitic granite obtained in this paper, but are significantly younger than the mylonitization ages (213–187 Ma) of the host rocks (J. X. Cai, 2012; K. J. Zhang & Cai, 2009). This suggests that gold mineralization in the Hetai goldfield is related to emplacement of the Wucun granite in the Late Jurassic rather than the mylonitization event in the Late Triassic during the Indosinian Orogeny.

It is important to note that although the gold mineralization in the Hetai goldfield is spatially associated with mylonitic zones and most of the orebodies have a consistent attitude with mylonitic foliations, the mineralized mylonites have low grades (0.2 to 0.7 g/t) unless overprinted by cataclastic structures (15.5 to 194.5 g/t). In addition, field investigation and microscopic observation indicate frequent crosscutting of mylonitic foliation by auriferous quartz veinlets (Figures 4d and 5h). Therefore, the main mineralization is probably related to cataclasis after mylonitization, in relation to brittle deformation in late Jurassic, when the Wucun pluton was emplaced.

6.2 | Origin of the ore-forming constituents

A magmatic origin for mineralizing fluids finds its support from the H–O isotopic composition. The H–O data obtained for sericite and chlorite from ores in this study fall mostly into the field of magmatic waters. Since these minerals are derived from the main mineralization stage, their H–O isotopic values indicate that magmatic hydrothermal fluids may be involved in the main ore-forming fluids for the Hetai goldfield. Our new H–O isotope data and distinct from previously published data that spread from metamorphic, magmatic to meteoric waters (Jiao, Wang, et al., 2017; W. Liu et al., 2005; Lu, 1993; Tu & Gao, 1991; H. N. Wang et al., 1989), lead to ambiguous interpretations about the origin(s) of the ore-forming fluids.

Sulphur and lead isotope studies also provide an efficient tool for determining and tracing the origin of these components in ore deposits. The lack of sulphate minerals and the presence of CH_4-bearing fluids in the Hetai goldfield suggest a reduced environment for the formation of the Au–Ag–Cu polymetallic ores. The sulphur isotopic

TABLE 3 Sulphur isotopic compositions of pyrites in Hetai ores (‰)

Sample	Location	$\delta^{34}S$	1SE
159GC02-01	Gaocun	−2.41	0.01
159GC02-02	Gaocun	−2.46	0.01
159GC02-03	Gaocun	−2.49	0.01
159GC02-04	Gaocun	−2.42	0.02
159GC02-06	Gaocun	−2.47	0.01
159GC02-07	Gaocun	−2.50	0.01
159GC02-08	Gaocun	−2.76	0.02
159GC02-09	Gaocun	−2.99	0.01
159GC02-10	Gaocun	−2.51	0.01
159GC02-11	Gaocun	−3.24	0.01
159GC02-12	Gaocun	−3.11	0.01
159GC02-13	Gaocun	−3.15	0.02
159GC02-14	Gaocun	−3.27	0.01
159GC02-15	Gaocun	−2.57	0.01
159GC02-16	Gaocun	−3.87	0.01
159HH02-01	Hehai	−4.26	0.01
159HH02-02	Hehai	−4.68	0.01
159HH02-03	Hehai	−4.04	0.01
159HH02-04	Hehai	−3.44	0.01
159HH02-05	Hehai	−4.44	0.02
159HH02-06	Hehai	−4.62	0.01
159HH02-07	Hehai	−5.09	0.01
159HH02-08	Hehai	−5.24	0.02
159HH02-09	Hehai	−4.12	0.01
159HH02-10	Hehai	−4.02	0.01
159HH02-11	Hehai	−4.36	0.02
159HH02-12	Hehai	−4.41	0.01
159HH02-13	Hehai	−4.31	0.01
159HH02-14	Hehai	−4.27	0.01
159HH02-15	Hehai	−4.68	0.02
159YX02-01	Yunxi	−3.59	0.01
159YX02-02	Yunxi	−3.57	0.01
159YX02-03	Yunxi	−3.49	0.01
159YX02-06	Yunxi	−3.15	0.01
159YX02-07	Yunxi	−2.74	0.01
159YX02-08	Yunxi	−1.47	0.02
159YX02-09	Yunxi	−1.94	0.02
159YX02-10	Yunxi	−3.04	0.01
159YX02-11	Yunxi	−2.32	0.02
159YX02-12	Yunxi	−1.50	0.01
159YX02-13	Yunxi	−3.46	0.02
159YX02-14	Yunxi	−3.71	0.01
159YX02-15	Yunxi	−3.37	0.01
159YX02-16	Yunxi	−3.39	0.01
159YX02-17	Yunxi	−3.36	0.01
159YX02-18	Yunxi	−3.45	0.01
159YX02-19	Yunxi	−3.40	0.01
159YX02-20	Yunxi	−3.44	0.01

(Continues)

TABLE 3 (Continued)

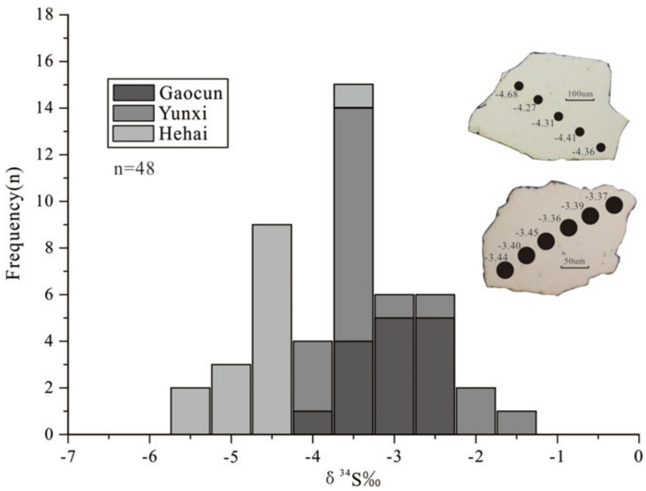

FIGURE 14 Histogram of the sulphur isotopic compositions of pyrites from auriferous silicified cataclastic ores [Colour figure can be viewed at wileyonlinelibrary.com]

fractionation between sulphides and fluids would be small at a low oxygen fugacity and medium-low temperature (Ohmoto, 1979) condition. In addition, a previous study (Fu, 1988) has shown that the $\delta^{34}S$ values of pyrite and chalcopyrite at Hetai are consistently larger than those of sphalerite and galena, indicating that sulphides were in equilibrium with ore fluids. Thus, the measured $\delta^{34}S_{VCDT}$ values of sulphides can be approximated as the total sulphur isotopic compositions of ore-forming fluids (Ohmoto, 1979). Pyrite from ores in the Hetai goldfield has $\delta^{34}S_{VCDT}$ values restricted to the interval of −5.2‰ to −1.5‰ (averaging −3.4‰; Figure 14). The narrow range indicates that sulphur was mainly derived from a single homogeneous source with average value close to that of magma (0 ± 5‰; Ohmoto, 1979). The slight negative values may be due to magma degassing that expels heavy ^{34}S in gaseous phase and leaves behind light ^{32}S in liquid phase (Ohmoto, 1979).

The diagram of $^{207}Pb/^{204}Pb$ versus $^{206}Pb/^{204}Pb$ (Figure 15a) shows that all ores and wall rocks are plotted near to or above the upper crust curve. The diagram of $^{208}Pb/^{204}Pb$ versus $^{206}Pb/^{204}Pb$ (Figure 15b) further displays that the analysed samples have a clear liner array approximately parallel to the orogen and upper crust curves. Therefore, the primary source of the lead in the Hetai goldfield was contributed by the upper crust reservoir and the orogen. The Pb isotopic compositions of sulphides in the ores from the Hetai goldfield are similar to those of the Wucun granite, rather than schists and migmatite in the area (Table 5 and Figure 15).

TABLE 4 Lead isotopic compositions of schist, migmatite, granite, and sulphides from the Hetai goldfield

Sample	Lithology	Object	$^{206}Pb/^{204}Pb$	$^{207}Pb/^{204}Pb$	$^{208}Pb/^{204}Pb$	Location	References
CM1501-14	schist	Wr	19.400	15.840	38.390	Gaocun	Lu, 1993
ZK1504-8	schist	Wr	19.460	15.850	38.320	Gaocun	
ZK1502-2	schist	Wr	19.720	15.940	38.520	Gaocun	
17HT-04B	schist	Wr	19.726	15.844	40.773	Gaocun	This study
159GC02	migmatite	Wr	13.712	15.474	38.583	Gaocun	
159GC04-1	migmatite	Wr	18.294	15.753	38.711	Gaocun	
159GC09	migmatite	Wr	18.038	15.746	38.995	Gaocun	
17GC01	migmatite	Wr	18.394	15.737	38.884	Gaocun	
17HT-02	Wucun granite	Wr	19.118	15.782	39.146	Wucun	
17HT-03	Wucun granite	Wr	17.665	15.580	38.607	Wucun	
17HT-05	Wucun granite	Wr	18.757	15.735	38.990	Wucun	
17HT-06	Wucun granite	Wr	18.803	15.739	38.975	Wucun	
G28-1	ore	Py	18.651	15.725	38.945	Taipingding	Fu, 1988
G29-2	ore	Py	18.855	15.743	39.216	Gaocun	
G30-7a	ore	Py	19.078	15.719	39.502	Gaocun	
G32-3a	ore	Py	19.635	15.737	39.001	Gaocun	
G35-3	ore	Py	19.014	15.747	39.314	Gaocun	
G38-7b	ore	Gn	18.776	15.728	39.128	Gaocun	
G42-16a	ore	Gn	18.828	15.732	39.178	Gaocun	
//	ore	Py	19.014	15.734	39.377	Gaocun	Tu & Gao, 1991
//	ore	Py	18.116	15.584	38.154	Gaocun	
//	ore	Py	18.651	15.725	38.945	Yunxi	
//	ore	Py	18.160	15.627	38.270	Yunxi	
//	ore	Py	18.694	15.691	38.868	Gaocun	
//	ore	Cp	18.770	15.740	39.314	Gaocun	
//	ore	Cp	18.601	15.600	38.578	Gaocun	
//	ore	Po	18.139	15.627	38.235	Yunxi	
//	ore	Po	18.930	15.790	39.300	Gaocun	
//	ore	Sp	18.929	15.862	39.602	Gaocun	
//	ore	Gn	18.798	15.695	39.056	Yunxi	
//	ore	Gn	18.840	15.737	39.135	Gaocun	
//	ore	Gn	18.809	15.723	39.090	Gaocun	
574	ore	Py	19.014	15.747	39.315	Gaocun	Lu, 1993
CM1501-4	ore	Gn	18.828	15.732	39.178	Gaocun	
14HT010	ore	Py	18.661	15.690	38.876	Gaocun −230	Jiao, Wang, et al., 2017
14HT053	ore	Py	18.536	15.644	38.746	Gaocun −140	
14HT066	ore	Py	18.855	15.705	39.131	Gaocun −90	
14HT073	ore	Py	18.890	15.707	39.066	Gaocun −40	
14HT078	ore	Py	18.480	15.700	38.864	Yunxi −140	
14HT087	ore	Py	19.087	15.793	39.410	Yunxi −140	
14HT078	ore	Cp	19.143	15.732	39.296	Yunxi −140	
14HT015	ore	Cp	18.638	15.681	38.862	Gaocun −230	
14HT088	ore	Po	18.608	15.675	38.897	Yunxi −140	
14HT092	ore	Po	19.404	15.744	39.597	Yunxi −90	
14HT101	ore	Po	18.939	15.665	38.936	Yunxi −90	
14HT103	ore	Po	18.642	15.659	38.976	Yunxi +110	
14HT104-1	ore	Po	18.412	15.681	38.777	Hetai	
14HT104-3	ore	Po	18.044	15.568	38.426	Hetai	

Note: Tr: whole-rock; Cp: chalcopyrite; Po: pyrrhotite; Py: pyrite; Gn: galena; Sp: sphalerite, //: not given.

Another point worth noting is that the mixing between meteoric waters and ore-forming fluids may have occurred in the late stage of mineralization. This is reflected on the H–O isotopic data of pyrophyllite from altered schist of the late substage of hydrothermal mineralization that fall in the field between meteoric and magmatic waters, which is consistent with the $\delta^{18}O$ values of calcite (−0.51‰ to 0.39‰; Lu, 1993). The mixing may also result in several scatters of the intermediate substage of mineralization stages that extend to relatively low δD values lying below the magmatic water field (Figure 13). Of course, degassing of deep-seated magma effect (Baker & Lang, 2001; Shinohara & Hedenquist, 1997) is another possible reason.

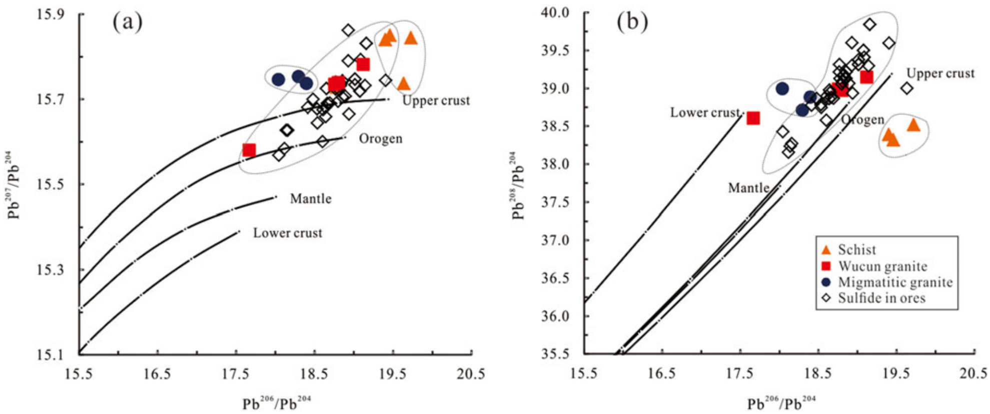

FIGURE 15 Lead isotopic compositions of sulphides and wall rocks from the Hetai goldfield. (a) $^{207}Pb/^{204}Pb$ vs. $^{206}Pb/^{204}Pb$ and (b) $^{208}Pb/^{204}Pb$ vs. $^{206}Pb/^{204}Pb$; the evolution curves of the upper crust, lower crust, mantle, and orogen are from Zartman and Doe (1981) [Colour figure can be viewed at wileyonlinelibrary.com]

TABLE 5 Sericite $^{40}Ar/^{39}Ar$ analyses of Hetai ore (HT104-3)

Stage	^{36}Ar(a)	^{37}Ar(Ca)	^{38}Ar(Cl)	^{39}Ar(k)	^{40}Ar(r)	Age ± 2σ (Ma)	^{40}Ar(r) (%)	^{39}Ar(k) (%)
1	0.0004	0.1528	0.0000	15.2666	201.7677	164.04 ± 1.09	99.9272	0.4175
2	0.0034	0.0843	0.0176	51.8947	690.3058	165.05 ± 0.78	99.8374	1.4193
3	0.0311	0.1880	0.6251	249.9327	3,295.7087	163.68 ± 0.63	99.7047	6.8355
4	0.0309	0.0000	1.0476	357.6685	4,649.0653	161.45 ± 0.62	99.7864	9.7820
5	0.0291	0.1362	0.9204	313.4972	4,057.9966	160.81 ± 0.62	99.7706	8.5740
6	0.0231	0.0832	0.4369	169.4849	2,206.9871	161.73 ± 0.64	99.6745	4.6353
7	0.0294	0.0000	0.4946	181.9927	2,431.8419	165.77 ± 0.65	99.6265	4.9774
8	0.0398	0.0945	0.8055	288.5999	3,821.8656	164.35 ± 0.63	99.6759	7.8931
9	0.0441	0.0000	1.0342	385.7905	4,949.5668	159.44 ± 0.63	99.7194	10.5512
10	0.0185	0.1565	0.4713	185.5367	2,385.4318	159.77 ± 0.62	99.7537	5.0743
11	0.0233	0.3214	1.1119	383.3302	4,914.5142	159.33 ± 0.61	99.8419	10.4839
12	0.0217	0.1057	0.8106	265.1192	3,395.0797	159.16 ± 0.65	99.7932	7.2509
13	0.0180	0.2202	0.7109	241.5241	3,090.2258	159.03 ± 0.61	99.8100	6.6056
14	0.0210	0.5118	1.0116	312.5403	3,993.4692	158.82 ± 0.66	99.8267	8.5478
15	0.0162	0.3647	0.7445	235.8236	3,024.8432	159.41 ± 0.69	99.8241	6.4497
16	0.0080	0.1942	0.0071	18.3742	235.5386	159.32 ± 0.87	98.9895	0.5025

The Hetai goldfield was previously regarded as being deposited from metamorphic hydrothermal fluids released during mylonitization of the Yunkai Group with greenschist-facies conditions (H. N. Wang et al., 1997; Y. Zheng et al., 2014). However, mineralizing fluids from magmatic origins were also proposed (Jiao, Wang, et al., 2017; Ye & Qiu, 1993). The C–O isotopic compositions ($\delta^{13}C_{PDB}$ ranging from −1.9‰ to −3.5‰ and $\delta^{18}O_{SMOW}$ from 9.0‰ to 10.6‰) of calcites from the ores of the Hetai goldfield (Jiao, Wang, et al., 2017) fall in or close to the mantle and primary igneous carbonatites fields, but far from the fields for marine carbonate and sedimentary organic matters. Noble gas isotope data provide further constraints on the source of ore fluid. The elevated $^{3}He/^{4}He$ ratios suggest the presence of mantle-derived fluid in the hydrothermal system (Jiao, Wang, et al., 2017). The $^{3}He/^{4}He$ ratios (0.27–0.62 Ra) of Au-bearing pyrite from the Hetai goldfield are lower than that of subcontinental lithospheric mantle He (6–9 Ra) but are one to two orders of magnitude higher than the crustal production He (0.01–0.05 Ra). Elemental and Sr–O isotope geochemistry studies showed that the Wucun pluton was produced by partial melting of the high-grade basement rocks and upper mantle materials (L. Wang et al., 2003), thus may explain the He isotopes observed in the Hetai goldfield. In addition, there is an intimate correlation of Au with Cu in the Hetai goldfield (Figure 7), which is inconsistent with the thermodynamic modelling of pelite metamorphic devolatilization (66% gold and 3% copper can be scavenged through

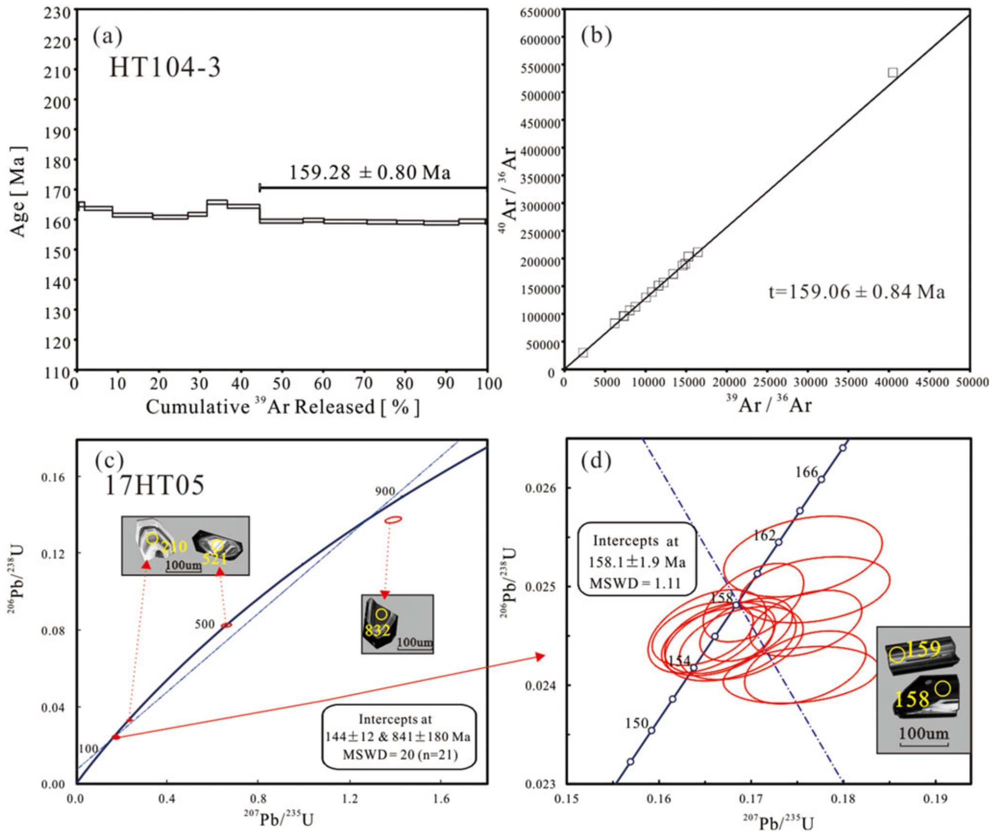

FIGURE 16 (a and b) $^{40}Ar/^{39}Ar$ age spectrums and isochron plot for sericite from Hetai ore; (c and d) Zircon U–Pb concordia diagrams and representative zircon CL images of the Wucun biotite monzonitic granite [Colour figure can be viewed at wileyonlinelibrary.com]

the chlorite dehydration process; R. Zhong, Brugger, Tomkins, Chen, & Li, 2015). Thus, a Cu-rich hydrothermal fluid could not be derived from the metamorphism of the host rocks. For these reasons, the Hetai goldfield is distinct from the typical orogenic gold deposits, which are characterized by mainly metamorphic water and base metal-poor metal assemblages (Groves, Goldfarb, Robert, & Hart, 2003; Kerrich, Goldfarb, Groves, Garwin, & Jia, 2000; Mccuaig & Kerrich, 1998; Phillips & Powell, 2010).

To sum up, H–O–S–Pb and noble gas isotopic compositions and geochronologic data suggest that the mineralization in the Hetai goldfield may be closely related to the magmatic activities. The ore fluids are mainly magmatic water, although there are minor contributions from other sources including mantle-derived fluids and meteoric water, and the sources of ore metals are probably mainly related to the Wucun granitic pluton.

6.3 | Evolution of ore-forming fluids and gold deposition processes

The overall trend of evolution of the ore-forming system is from high temperatures to low temperatures (Figure 11). The syntectonic metamorphic stage is characterized by fluid inclusion homogenization temperatures between 350°C and 400°C, which is consistent with distortion of plagioclase twins, which reflects ductile deformation at a temperature of ca. 450 ± 50°C (Tullis & Yund, 1987). The homogenization temperatures and salinities of ore-forming fluids have a lowering trend following hydrothermal mineralization (Table 1; temperature: from 250–320°C decrease to 110–207°C; salinity: from 2.6- to 12.9-wt.% NaCl equiv. decrease to 0.2- to 7.3-wt.% NaCl equiv.).

The change from ductile deformation associated with mylonitization to brittle deformation associated with cataclasis reflects a decrease of pressure, possibly related to the transition from lithostatic to hydrostatic pressure conditions (Sibson, Robert, & Poulsen, 1988). A drop of fluid pressure may make the fluid evolve from one-phase region into the two-phase region and trigger fluid immiscibility/boiling (Goldstein & Reynolds, 1994), which is also supported by the petrographic evidence in Hetai goldfield: the coexistence (Figure 9h,i) of CO_2-bearing (type 2a) and CO_2-rich (type 3) inclusions in the main mineralization stage. More importantly, two types of those inclusions homogenized at the similar temperature range but different phase: the type 2a inclusions are into liquid and the type 3 inclusions are into carbonic phase, respectively.

Gold precipitation from hydrothermal fluids may be caused by cooling, decompression, phase separation (or boiling), interaction with rocks, and mixing with external waters (Garofalo & Ridley, 2014). A decrease in the activity of HS^- and fO_2 and an increase in pH, which

TABLE 6 LA-ICP-MS U–Pb isotopic data of zircon grains in biotite monzonitic granite sample (17HT05) from Wucun pluton

	Th	U		Isotope ratios						Apparent ages (Ma)						Concord
Spot No.	(ppm)		Th/U	$^{207}Pb/^{206}Pb$	1σ	$^{207}Pb/^{235}U$	1σ	$^{206}Pb/^{238}U$	1σ	$^{207}Pb/^{206}Pb$	1σ	$^{207}Pb/^{235}U$	1σ	$^{206}Pb/^{238}U$	1σ	(%)
17HT05-01	928	6526	0.14	0.05371	0.00129	0.18225	0.00459	0.02446	0.00021	366.7	53	169.9	4	155.8	1	91
17HT05-03	376	2221	0.17	0.05167	0.00162	0.17538	0.00555	0.02410	0.00019	333.4	72	164.1	5	153.5	1	93
17HT05-06	1023	370	2.76	0.05781	0.00151	0.65914	0.01779	0.08268	0.00076	524.1	62	514.1	10	512.1	4	99
17HT05-07	467	1104	0.42	0.04988	0.00137	0.16776	0.00468	0.02445	0.00027	190.8	65	157.5	4	155.7	2	93
17HT05-08	583	1902	0.31	0.05142	0.00154	0.17693	0.00535	0.02497	0.00022	261.2	69	165.4	5	159.0	1	93
17HT05-09	352	2228	0.16	0.04938	0.00115	0.16635	0.00401	0.02444	0.00023	164.9	56	156.2	3	155.7	1	93
17HT05-11	538	3187	0.17	0.05179	0.00116	0.17593	0.00400	0.02463	0.00022	276.0	47	164.5	3	156.8	1	93
17HT05-12	68	1781	0.04	0.07302	0.00150	1.38795	0.02903	0.13771	0.00132	1014	42	883.8	12	831.8	7	93
17HT05-14	163	1115	0.15	0.05470	0.00164	0.17890	0.00538	0.02375	0.00026	398.2	66	167.1	4	151.3	2	90
17HT05-15	1059	1019	1.04	0.05485	0.00177	0.18366	0.00563	0.02443	0.00026	405.6	72	171.2	5	155.6	2	90
17HT05-19	448	2146	0.21	0.05045	0.00169	0.17562	0.00567	0.02530	0.00027	216.7	50	164.3	5	161.1	2	93
17HT05-20	52	115	0.46	0.05237	0.00363	0.17783	0.01052	0.02387	0.00040	301.9	154	166.2	9	152.0	3	91
17HT05-27	303	279	1.09	0.05184	0.00206	0.23531	0.00844	0.03315	0.00036	279.7	92	214.6	7	210.2	2	97
17HT05-28	950	5489	0.17	0.04978	0.00096	0.16945	0.00331	0.02456	0.00021	183.4	44	158.9	3	156.4	1	93
17HT05-29	481	4884	0.10	0.04943	0.00093	0.17024	0.00360	0.02484	0.00026	168.6	44	159.6	3	158.2	2	93
17HT05-30	182	1471	0.12	0.04987	0.00121	0.16892	0.00443	0.02443	0.00024	187.1	56	158.5	4	155.6	2	93
17HT05-31	1102	4553	0.24	0.05242	0.00116	0.17586	0.00435	0.02418	0.00024	305.6	50	164.5	4	154.0	2	93
17HT05-35	965	3681	0.26	0.04837	0.00102	0.16473	0.00362	0.02452	0.00021	116.8	50	154.8	3	156.2	1	93
17HT05-36	608	3944	0.15	0.04897	0.00113	0.16660	0.00397	0.02448	0.00024	146.4	49	156.5	3	155.9	1	93
17HT05-39	396	3302	0.12	0.04910	0.00124	0.16521	0.00422	0.02455	0.00028	153.8	55	155.3	4	156.3	2	93

end result are rapid saturation of hydrothermal fluids with respect to Au (Williams-jones, Bowell, & Migdisov, 2009). Based on the fluid inclusion and stable isotope data, phase separation (or fluid immiscibility) and mixing with meteoric water are the most likely the reasons of gold precipitation in the Hetai goldfield. Because CO_2 can produce weak acidity in aqueous solutions, it can adjust pH values of ore-forming fluids to keep gold-hydrosulphide complex stable during gold transportation (Phillips & Evans, 2004). However, phase separation or fluid immiscibility lead to an increase in pH of the liquid phase due to preferential partitioning of CO_2 into the vapour and thus gives rise to Au precipitation (Williams-jones et al., 2009). Another important effect of fluid immiscibility is removal of H_2S and CO_2 into the vapour phase, which also leads to breakdown of Au-hydrogen sulphide complexes and may result in gold precipitation (e.g., Simmons, White, & John, 2005). On the other hand, mixing of gold-bearing hydrothermal fluid with meteoric waters leads primarily to dilution and oxidation. Based on thermodynamic modeling, a relatively small increase in fO_2 leads to a precipitous drop in HS^- concentration and consequently in gold solubility (Williams-jones et al., 2009; references therein).

6.4 | Metallogenic model

The above lines of evidence indicate that gold deposits in the Hetai goldfield formed from fluids associated with granitic magmatism in the Late Jurassic. Although further research is needed, a new scheme of tectonic–magmatic evolution is proposed for the metallogeny of the Hetai goldfield.

In the latest Neo-Proterozoic, a suite of clastic rocks, that is, the Yunkai Group, was deposited within a continental rift between the Cathaysia and Yangtze blocks. The sequence has some similarities to exhalative sedimentary processes in modern ocean floor, which are rich in elements Au, Ba, S, As, Ag, Cu, Ni, and Co (Lu, 1993; H. N. Wang et al., 1989). Several thermal events were superimposed on the Yunkai clastic rocks and resulted in schists (7.8 ppb Au), migmatite (5.8 ppb Au), and even gneiss (4 ppb Au) with decreasing Au contents (Dai, 1989), implying that Au was lost during prograde metamorphism (J. Chen & Wang, 1994; Lu, 1993). Among these episodes of tectonic events, two imparted regional metamorphism to the Yunkai Group that occurred in the Phanerozoic, corresponding to the Caledonian and Indosinian orogenies, respectively (Lin et al., 2008; Y. Wang, Fan, Zhang, & Zhang, 2013; G. W. Zhang et al., 2013). The Caledonian (ca. 455–423 Ma) tectonothermal event was recorded by minor amounts of migmatite and granite (S. B. Peng, Jin, Liu, et al., 2006; Wan et al., 2010; L. Wang et al., 2003; Y. Wang, Fan, Zhao, et al., 2007; L. Wang, Long, & Zhou, 2013). This event is also recorded by inherited zircons (Wan et al., 2010) from voluminous magmatites and granites of the Indosinian (ca. 245–205 Ma) distributed in the Hetai district (S. B. Peng, Jin, Liu, et al.,

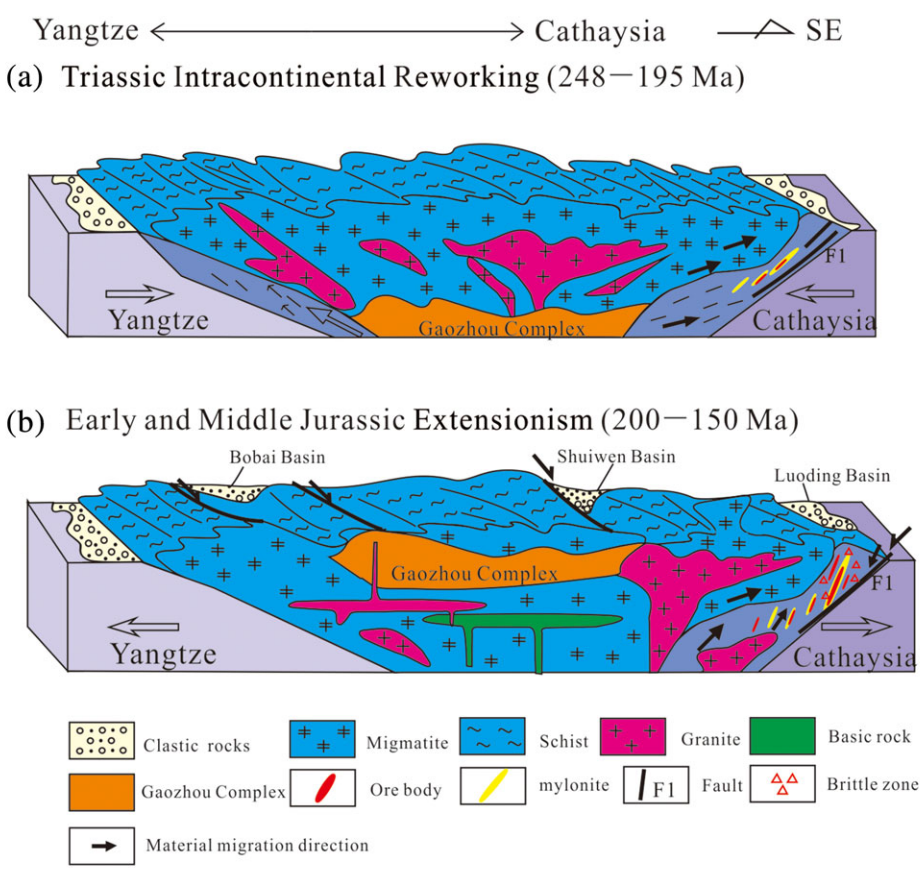

FIGURE 17 Metallogenic model for the Hetai goldfield (modified from Y. Wang, Fan, Cawood, et al., 2007) [Colour figure can be viewed at wileyonlinelibrary.com]

2006; S. B. Peng, Wang, Wei, et al., 2006; L. Wang et al., 2003; L. Wang, Long, & Zhou, 2013). These tectonothermal episodes may have caused preliminary transfer of Au from schist, migmatite, and gneiss to structural weak zones, such as regional faults (i.e., Baoyatang–Kengwei fault) and ductile shear zones (with mylonitization; Figure 17a). Subsequently, the Yanshanian Orogeny and associated granitic intrusions contributed most of the gold in the Hetai goldfield. Most granitic intrusions in the Hetai goldfield are of the Late Yanshanian (Cretaceous) ages, and a few of them (including the Wucun pluton) yield Early Yanshanian (Middle to Late Jurassic) ages (L. Wang et al., 2003; Zhai et al., 2005). The Wucun granite is not only spatially close to the goldfield but also temporally close to the metallogenic age. Its emplacement may have brought in vast magmatic–hydrothermal fluids and ore-forming constituents to overprint the weak preceding mineralization in structural zones, acted as cataclasis-reactivated mylonitic belts, where Au precipitation occurred. Moreover, with the increasing development of cataclasis in the shear zones, meteoric waters were increasingly added into the ore fluids towards the late substage of the hydrothermal stage of mineralization, further contributing to Au precipitation (Figure 17b).

7 | CONCLUSIONS

1. The gold mineralization occurred at ca. 159 Ma, which is essentially contemporaneous with the emplacement of the Wucun granitic pluton.
2. The ore-forming fluids are most likely dominated by magmatic water, with some contributions from the meteoric water, while the ore metals probably derived from the Wucun intrusion as well as the Yunkai Group host rocks.
3. The Hetai goldfield experienced three mineralization stages: syntectonic metamorphic stage, hydrothermal stage, and supergene stage, and the hydrothermal stage is the main ore-forming stage.
4. Fluid inclusion study suggests that the ore-forming fluids evolved from relatively high temperatures and salinities to relatively low temperatures and salinities, and fluid immiscibility and/or mixing may have played important roles in Au precipitation.

ACKNOWLEDGEMENTS

We would like to thank Prof Guoxiang Chi for his constructive suggestions on fluid inclusions work. Yuhang Jiang and Lingjun Zeng are thanked for their assistance with fluid inclusion analyses and data processing. This study is co-funded by the National Key R&D Program of China (No. 2016YFC0600401), the National Natural Science Foundation of China (No. 41472171), and the China Geological Survey (No. 12120114052801).

ORCID

Lixing Wang https://orcid.org/0000-0002-3240-6959

REFERENCES

Bai, X. J., Wang, M., Jiang, Y., & Qiu, H. (2013). Direct dating of tin-tungsten mineralization of the piaotang tungsten deposit, South China, by $^{40}Ar/^{39}Ar$ progressive crushing. *Geochimica et Cosmochimica Acta*, *114*, 1–12. https://doi.org/10.1016/j.gca.2013.03.022

Baker, T., & Lang, J. R. (2001). Reconciling fluid inclusion types, fluid processes, and fluid sources in skarns: An example from the Bismark Deposit, Mexico. *Mineralium Deposita*, *38*, 474–495.

Brown, P. E., & Hagemann, S. G. (1995). MacFlinCor and its application to fluids in Archean lode-gold deposits. *Geochimica et Cosmochimica Acta*, *59*, 3943–3952. https://doi.org/10.1016/0016-7037(95)00254-W

Cai, J. X. (2012). Hetai dextral ductile shear zone, Western Guangdong, and its controlling on formation of gold deposit. *Geological Review*, *58*, 1069–1080. (in Chinese with English abstract).

Cai, J. X. (2013). An Early Jurassic dextral strike-slip system in southern South China and its tectonic significance. *Journal of Geodynamics*, *63*, 27–44. https://doi.org/10.1016/j.jog.2012.09.003

Cai, M., Zhan, M., Peng, S., Meng, X., & Liu, G. (2002). Study of mesozoic metallogenic geological setting and dynamic mechanism in Yunkai area. *Mineral Deposits*, *21*, 264–269. (in Chinese with English abstract).

Chen, C. H., Hsieh, P. S., Lee, C. Y., & Zhou, H. W. (2011). Two episodes of the Indosinian thermal event on the South China Block: Constraints from LA-ICPMS U–Pb zircon and electron microprobe monazite ages of the Darongshan S-type granitic suite. *Gondwana Research*, *19*, 1008–1023. https://doi.org/10.1016/j.gr.2010.10.009

Chen, J., & Wang, H. (1994). Distribution of REE and other trace elements in the Hetai gold deposit of South China: Implications for evolution of an auriferous shear zone. *Journal of Southeast Asian Earth Sciences*, *10*, 217–226. https://doi.org/10.1016/0743-9547(94)90021-3

Clayton, R. N., & Mayeda, T. K. (1963). The use of bromine pentafluoride in the extraction of oxygen from oxides and silicates for isotopic analysis. *Geochimica et Cosmochimica Acta*, *27*, 43–52. https://doi.org/10.1016/0016-7037(63)90071-1

Coleman, M. L., Shepherd, T. J., Durham, J. J., Rouse, J. E., & Moore, G. R. (1982). Reduction of water with zinc for hydrogen isotope analysis. *Analytical Chemistry*, *54*, 993–995. https://doi.org/10.1021/ac00243a035

Dai, A. (1989). Sinian gold-bearing formation and its relation with gold mineralization, West Guangdong Province. *Journal of Nanjing Institute of Geology and Mineral Resources, Chinese Academy of Geological Sciences*, *106*(3), 71–85. (in Chinese with English abstract)

Diamond, L. W. (2001). Review of the systematic of CO_2–H_2O fluid inclusions. *Lithos*, *55*, 69–99. https://doi.org/10.1016/S0024-4937(00)00039-6

Duan, J., He, S., & Zhou, C. (1992). On the structural characteristics of Hetai gold-deposit Guangdong and the gold-deposit model of shear zone type. *Journal of Central South University*, *23*, 245–253. (in Chinese with English abstract)

Fu, L. (1988). Gold mineralization and metamorphism in Hetai goldfield, Guangdong Province. *Guangdong Research Report*. Guangzhou, China: Guangdong Geoscience Institute, pp. 11–68 (in Chinese).

Garofalo, P. S., & Ridley, J. R. (2014). *Gold-transporting hydrothermal fluids in the earth's crust* (Vol. 402). Geological Society London Special Publications, pp. 9–70.

GBGMR (Guangdong Bureau of Geology and Mineral Resources) (1988). *Regional geology of Guangdong Province* (pp. 1–846). Beijing, China: Geological Publishing House. (in Chinese with English abstract).

GGB (Guangdong Geological Bureau) (2016). Gold-polymetal deposit integrated exploration area special geologic mapping and technology application demonstration in Hetai district. *Research Report*.

Guangzhou, China: Guangzhou institute of Geochemistry, pp. 68–71 (in Chinese).

Gilbert, S. E., Danyushevsky, L. V., Rodemann, T., Shimizu, N., Gurenko, A., Meffre, S., … Death, D. (2014). Optimisation of laser parameters for the analysis of sulphur isotopes in sulphide minerals by laser ablation ICP-MS. *Journal of Analytical Atomic Spectrometry*, *29*, 1042–1051. https://doi.org/10.1039/C4JA00011K

Goldstein, R. H., & Reynolds, T. J. (1994). *Systematics of fluid inclusions in diagenetic minerals*. *SEPM Short Course 31*. Oklahoma, (pp. 1–199).

Groves, D. I., Goldfarb, R. J., Robert, F., & Hart, C. J. R. (2003). Gold deposits in metamorphic belts: Overview of current understanding, outstanding problems, future research, and exploration significance. *Economic Geology*, *98*, 1–29.

Hart, C. J. R. (2007). Reduced intrusion-related gold systems. In W. D. Goodfellow (Ed.), *Mineral deposits of Canada: A synthesis of major deposit types, district metallogeny, the evolution of geological provinces, and exploration methods* (Vol. 5) (pp. 95–112). Geological Association of Canada, St. John's, Newfoundland, Mineral Deposits Division, Special Publication.

He, S., Duan, J., Zhou, C., & Peng, S. (1992). On the gold-deposit of shear zone-type and its classification. *Transactions of Nonferrous Metals Society of China*, *2*, 1–6.

He, W. (1993). Physical-chemical conditions for the ore-forming process of the Hetai gold deposit in Guangdong province and ore-prospecting directions. *Mineral Deposits*, *12*, 120–128. (in Chinese with English abstract).

Jiang, Y., Niu, H., Zhao, Y., Bao, Z., Li, N., & Shan, Q. (2017). Fluid inclusion and stable isotopic constraints on fluid sources and evolution of the Luojiahe Cu deposit in the southern margin of the North China Craton. *Ore Geology Reviews*, *80*, 214–228. https://doi.org/10.1016/j.oregeorev.2016.06.028

Jiao, Q. Q., Deng, T., Wang, L. X., Xu, D. R., Chi, G. X., Chen, G. W., … Zou, S. H. (2017). Geochronological and mineralogical constraints on mineralization of the Hetai goldfield in Guangdong Province, South China. *Ore Geology Reviews*, *88*, 655–673. https://doi.org/10.1016/j.oregeorev.2017.03.002

Jiao, Q. Q., Wang, L. X., Deng, T., Xu, D. R., Chen, G. W., Yu, D. S., … Gao, Y. W. (2017). Origin of the ore-forming fluids and metals of the Hetai goldfield in Guangdong Province of South China: Constraints from C-H-O-S-Pb-He-Ar isotopes. *Ore Geology Reviews*, *88*, 674–689. https://doi.org/10.1016/j.oregeorev.2017.04.005

Kerrich, R., Goldfarb, R., Groves, D., Garwin, S., & Jia, Y. (2000). The characteristics, origins, and geodynamic settings of supergiant gold metallogenic provinces. *Science China Earth Sciences*, *43*, 1–68. https://doi.org/10.1007/BF02911933

Koppers, A. A. P. (2002). ArArCAlC—Software for $^{40}Ar/^{39}Ar$ age calculations. *Computers & Geosciences*, *28*, 605–619. https://doi.org/10.1016/S0098-3004(01)00095-4

Li, C. Y., Zhang, H., Wang, F. Y., Liu, J. Q., Sun, Y. L., Hao, X. L., … Sun, W. D. (2012). The formation of the Dabaoshan porphyry molybdenum deposit induced by slab rollback. *Lithos*, *150*, 101–110. https://doi.org/10.1016/j.lithos.2012.04.001

Li, R., Chen, H., Xia, X., Yang, Q., Li, L., & Xu, J. (2017). Ore fluid evolution in the giant marcona Fe-(Cu) deposit, Perú: Evidence from in-situ sulfur isotope and trace element geochemistry of sulfides. *Ore Geology Reviews*, *86*, 624–638. https://doi.org/10.1016/j.oregeorev.2017.03.025

Li, Z. X., Li, X. H., Wartho, J. A., Clark, C., Li, W. X., & Zhang, C. L. (2010). Magmatic and metamorphic events during the Early Paleozoic Wuyi-Yunkai orogeny, southeastern South China: New age constraints and pressure-temperature conditions. *Geological Society of America Bulletin*, *122*, 772–793. https://doi.org/10.1130/B30021.1

Lin, W., Wang, Q., & Chen, K. (2008). Phanerozoic tectonics of south China block: New insights from the polyphase deformation in the Yunkai massif. *Tectonics*, *27*, 226–242.

Liu, W., Huang, M. X., & Ouyang, Y. F. (2005). Characteristics of mineralization fluids in the Hetai gold deposit of Guangdong. *Mineral Resources & Geology*, *19*, 469–474. (in Chinese with English abstract).

Liu, Y. S., Hu, Z. C., Gao, S., Günther, D., Xu, J., Gao, C. G., & Chen, H. H. (2008). In situ analysis of major and trace elements of anhydrous minerals by LA-ICP-MS without applying an internal standard. *Chemical Geology*, *257*, 34–43. https://doi.org/10.1016/j.chemgeo.2008.08.004

Lu, J. J. (1993). A geochemical study on metallogenesis of Hetai gold deposit in ductile shear zone, Guangdong province. *Journal of Nanjing University (Natural Sciences Edition)*, *29*, 293–302. (in Chinese with English abstract).

Lu, J. J., Wang, H. N., Shen, W. Z., & Dai, A. H. (1990). Study on isotope geology of Hetai gold deposit. *Contributions to Geology and Mineral Resources Research*, *5*, 84–92. (in Chinese with English abstract).

Ludwig, K. R. (2003). *Isoplot 3.00: A geochronological toolkit for Microsoft Excel*. Berkeley, America: Berkeley Geochronology Center.

Mao, J., Cheng, Y., Chen, M., & Pirajno, F. (2013). Major types and time-space distribution of Mesozoic ore deposits in South China and their geodynamic settings. *Mineralium Deposita*, *48*, 267–294.

Mccuaig, T. C., & Kerrich, R. (1998). P—T—t—deformation-fluid characteristics of lode gold deposits: Evidence from alteration systematics. *Ore Geology Reviews*, *12*, 381–453. https://doi.org/10.1016/S0169-1368(98)00010-9

McDougall, I., & Harrison, T. M. (1999). *Geochronology and thermochronology by the $^{40}Ar/^{39}Ar$ method* (pp. 1–269). Oxford: Oxford University Press.

Molnár, F., Mänttäri, I., O'Brien, H., Lahaye, Y., Pakkanen, L., Johanson, B., … Sakellaris, G. (2016). Boron, sulphur and copper isotope systematics in the orogenic gold deposits of the Archaean Hattu schist belt, Eastern Finland. *Ore Geology Reviews*, *77*, 133–162. https://doi.org/10.1016/j.oregeorev.2016.02.012

Ohmoto, H. (1979). Isotopes of sulfur and carbon. In *Geochemistry of hydrothermal ore deposits* second ed. New York: Wiley-Interscience, (pp. 509–567).

Peng, B. X., Wang, Y. J., Fan, W. M., Peng, T. P., & Liang, X. Q. (2006). LA-ICPMS zircon U–Pb dating for three typical granitic plutons from Central Hunan and western Guangdong Provinces and its petrogenetic implications. *Acata Geologica Sinica*, *80*(5), 660–669. (in Chinese with English abstract).

Peng, S. B., Jin, Z. M., Liu, Y. H., Fu, J. M., He, L. Q., & Cai, M. H. (2006). Petrochemistry, chronology and tectonic setting of strong peraluminous anatectic granitoids in Yunkai Orogenic Belt, Western Guangdong Province, China. *Journal of Earth Science*, *17*, 1–12. (in Chinese with English abstract).

Peng, S. B., Wang, Y., Wei, M., Peng, T., & Liang, X. (2006). LA-ICPMS zircon U-Pb dating for three Indosinian Granitic plutons from Central Hunan and Western Guangdong Provinces and its petrogenetic implications. *Acta Geologica Sinica*, *80*, 660–669. (in Chinese with English abstract).

Phillips, G. N., & Evans, K. A. (2004). Role of CO_2 in the formation of gold deposits. *Nature*, *429*, 860–863. https://doi.org/10.1038/nature02644

Phillips, G. N., & Powell, R. (2010). Formation of gold deposits: A metamorphic devolatilization model. *Journal of Metamorphic Geology*, *28*, 689–718. https://doi.org/10.1111/j.1525-1314.2010.00887.x

Pirajno, F., & Bagas, L. (2002). Gold and silver metallogeny of the South China Fold Belt: A consequence of multiple mineralizing events? *Ore*

Geology Reviews, *20*, 109–126. https://doi.org/10.1016/S0169-1368(02)00067-7

Shinohara, H., & Hedenquist, J. W. (1997). Constraints on magma degassing beneath the far southeast porphyry Cu–Au deposit, Philippines. *Journal of Petrology*, *38*, 1741–1752. https://doi.org/10.1093/petroj/38.12.1741

Shu, L. S., Faure, M., Yu, J. H., & Jahn, B. M. (2011). Geochronological and geochemical features of the Cathaysia block (South China): New evidence for the Neoproterozoic breakup of Rodinia. *Precambrian Research*, *187*, 263–276. https://doi.org/10.1016/j.precamres.2011.03.003

Sibson, R. H., Robert, F., & Poulsen, K. H. (1988). High-angle reverse faults, fluid-pressure cycling, and mesothermal gold-quartz deposits. *Geology*, *16*(6), 551–555. https://doi.org/10.1130/0091-7613(1988)016<0551:HARFFP>2.3.CO;2

Simmons, S. F., White, N. C., & John, D. A. (2005). Geological characteristics of epithermal precious and base metal deposits. *Economic Geology*, *100*, 485–522.

Steele-Macinnis, M., Lecumberri-Sanchez, P., & Bodnar, R. J. (2012). Short note: HokieFlincs_H_2O-NaCl: A Microsoft Excel spreadsheet for interpreting microthermometric data from fluid inclusions based on the PVTX properties of H_2O-NaCl. *Computers & Geosciences*, *49*, 334–337. https://doi.org/10.1016/j.cageo.2012.01.022

Tu, S., & Gao, Y. (1991). Mineralization characteristic and stable isotope constitutions of the Gaocun and Yunxi deposits in the Hetai goldfield, Guangdong province. *Acta Geoscientia Sinica*, *22*, 103–116. (in Chinese with English abstract).

Tullis, J., & Yund, R. A. (1987). Transition from cataclastic flow to dislocation creep of feldspar: Mechanisms and microstructure. *Geology*, *15*, 606–609. https://doi.org/10.1130/0091-7613(1987)15<606:TFCFTD>2.0.CO;2

Ushikubo, T., Williford, K. H., Farquhar, J., Johnston, D. T., Van Kranendonk, M. J., & Valley, J. W. (2014). Development of in situ sulfur four-isotope analysis with multiple Faraday cup detectors by SIMS and application to pyrite grains in a Paleoproterozoic glaciogenic sandstone. *Chemistry Geology*, *383*, 86–99. https://doi.org/10.1016/j.chemgeo.2014.06.006

Wan, Y., Liu, D., Wilde, S. A., Cao, J., Chen, B., & Dong, C. (2010). Evolution of the Yunkai Terrane, South China: Evidence from SHRIMP zircon U–Pb dating, geochemistry and Nd isotope. *Journal of Asian Earth Sciences*, *37*, 140–153. https://doi.org/10.1016/j.jseaes.2009.08.002

Wang, C., Zhang, C., Wang, Y., Qiu, X., & Gong, C. (2012). Chronological research of the Hetai gold mine in Gaoyao county, Guangdong province. *Geotectonica et Metallogenia*, *36*, 427–433. (in Chinese with English abstract).

Wang, H. N., Chen, J., Ji, J. F., & Qu, X. M. (1997). Geological and geochemical characteristics of the Hetai gold deposit, South China: Gold mineralization in an auriferous shear zone. *International Geology Review*, *39*, 181–190.

Wang, H. N., Zhang, J., Dai, A., Lin, J., Chen, C., & Ji, M. (1989). Geochemistry of the Hetai gold deposit in the altered mylonite zone. *Mineral Deposits*, *8*, 61–71. (in Chinese with English abstract).

Wang, L., Long, W. G., & Zhou, D. (2013). Zircon LA-ICP-MS U-Pb age of Caledonian granites from Precambrian basement in Yunkai area and its geological implications. *Geology in China*, *40*, 1016–1029. (in Chinese with English abstract).

Wang, L., Sha, L., Xu, W., Deng, G. Q., Zhang, S., & Liang, Y. (2003). *The theory of granite formation and series (Instanced in the granite of Hetai Area and West Guangding Province in South China)—And discussion on genetic classification of granite by three grades* (pp. 15–27). Guangzhou, China: Guangdong Science&Technology Press. (in Chinese with English abstract).

Wang, S. L. (2000). Prediction,prospecting and economic significancy of the bonanzas at Hetai Gold Mine. *Southern Iron and Steel*, *115*, 13–17. (in Chinese with English abstract).

Wang, Y., Fan, W., Cawood, P. A., Ji, S., Peng, T., & Chen, X. (2007). Indosinian high-strain deformation for the Yunkaidashan tectonic belt, South China: Kinematics and $^{40}Ar/^{39}Ar$ geochronological constraints. *Tectonics*, *26*, 229–247.

Wang, Y., Fan, W., Zhang, G., & Zhang, Y. (2013). Phanerozoic tectonics of the South China Block: Key observations and controversies. *Gondwana Research*, *23*, 1273–1305. https://doi.org/10.1016/j.gr.2012.02.019

Wang, Y., Fan, W., Zhao, G., Ji, S., & Peng, T. (2007). Zircon U–Pb geochronology of gneissic rocks in the Yunkai massif and its implications on the Caledonian event in the South China Block. *Gondwana Research*, *12*, 404–416. https://doi.org/10.1016/j.gr.2006.10.003

Wang, Y., Wu, C., Zhang, A., Fan, W., Zhang, Y., & Zhang, Y. (2012). Kwangsian and indosinian reworking of the eastern south china block: constraints on zircon U–Pb geochronology and metamorphism of amphibolites and granulites. *Lithos*, *150*(5), 227–242. https://doi.org/10.1016/j.lithos.2012.04.022

Williams-jones, A. E., Bowell, R. J., & Migdisov, A. A. (2009). Gold in solution. *Elements*, *5*(5), 281–287. https://doi.org/10.2113/gselements.5.5.281

Wu, G. Y. (1986). Geochronology of the Guangning granitoid complex. *Guangdong Geology*, *1*, 1–22. (in Chinese).

Wu, Y. B., & Zheng, Y. F. (2004). Study on zircon in mineralgeny and the constraints on the interpretation of U-Pb ages. *Chinese Science Bulletin*, *49*(16), 1589–1604. (in Chinese).

Ye, J. H., & Qiu, X. P. (1993). Geology and geochemistry study and metallogenic model research of Hetai gold province. *Journal of Precious Metallic Geology*, *2*, 306–315. (in Chinese with English abstract).

Zartman, R. E., & Doe, B. R. (1981). Plumbotectonics—The model. *Tectonophysics*, *75*, 135–162. https://doi.org/10.1016/0040-1951(81)90213-4

Zeng, J. (1986). The discovery and geological features of Hetai gold deposit in Guangdong province. *Contributions to Geology & Mineral Resources Research*, *1*, 55–60. (in Chinese with English abstract).

Zhai, W., Li, Z. L., Sun, X. M., Huang, D. L., Liang, J. L., & Miao, L. C. (2006). SHRIMP zircon U-Pb dating of the Hetai gold deposit in western Guangdong, China and geological implications. *Geological Review*, *52*, 690–699. (in Chinese with English abstract).

Zhai, W., Yuan, G., Li, Z. L., & Huang, D. (2005). U-Pb isotope age of zircons in gold-bearing quartz veins from the Hetai gold deposit, Western Guangdong, China: Constraints on the timing of gold metallogenesis. *Geological Review*, *51*, 340–346. (in Chinese with English abstract).

Zhang, B. Y., & Yu, H. N. (1992). The genetic relationship of mylonites, migmatites and granites with special preference to the deep-level nappe structure in Western Guangdong. *Geological Review*, *38*, 407–413. (in Chinese with English abstract).

Zhang, G. L., Boulter, C. A., & Liang, J. C. (2001). Brittle origins for disseminated gold mineralization in mylonite: Gaocun gold deposit, Hetai goldfield, Guangdong Province, South China. *Economic Geology*, *96*, 49–59.

Zhang, G. W., Guo, A. L., Wang, Y. J., Li, S. Z., Dong, Y. P., & Liu, S. F. (2013). Tectonics of South China continent and its implications. *Science China Earth Sciences*, *56*, 1804–1828. (in Chinese with English abstract), https://doi.org/10.1007/s11430-013-4679-1

Zhang, K. J., & Cai, J. X. (2009). NE-SW-trending Hepu-Hetai dextral shear zone in southern China: Penetration of the Yunkai Promontory of

South China into Indochina. *Journal of Structural Geology*, *31*, 737–748. https://doi.org/10.1016/j.jsg.2009.04.012

Zhang, L. G. (1989). *Petrogenic and minerogenic theories and prospecting* (pp. 1–200). Beijing, China: Beijing University of Technology Press. (in Chinese).

Zhao, Z., & Zheng, Y. (2000). Argon and Hydrogen diffusion compensation and estimation of their diffusivity in natural minerals. *Earth Science Frontiers*, *2*, 367–380. (in Chinese with English abstract).

Zheng, Y., Zhou, Y. Z., Wang, Y. J., Shen, W. J., Yang, Z. J., & Li, X. Y. (2014). A fluid inclusion study of the Hetai goldfield in the Qinzhou Bay-Hangzhou Bay metallogenic belt, South China. *Ore Geology Reviews*, *73*, 346–353.

Zheng, Y. F. (1993). Calculation of oxygen-isotope fractionation in hydroxyl-bearing silicates. *Earth and Planetary Science Letters*, *120*, 247–263. https://doi.org/10.1016/0012-821X(93)90243-3

Zheng, Y. F. (1998). Oxygen isotope fractionation between hydroxide minerals and water. *Physics and Chemistry of Minerals*, *25*, 213–221. https://doi.org/10.1007/s002690050105

Zheng, Y. F., & Chen, J. F. (2000). *Stable isotope geochemistry* (pp. 58–59). Beijing, China: Beijing Science Press. (in Chinese).

Zhong, R., Brugger, J., Tomkins, A. G., Chen, Y., & Li, W. (2015). Fate of gold and base metals during metamorphic devolatilization of a pelite. *Geochimica et Cosmochimica Acta*, *171*, 338–352. https://doi.org/10.1016/j.gca.2015.09.013

Zhong, Z. Q., Zhou, H. W., & You, Z. D. (1997). Shear zone arrays in Yunkai uplifted area and its relationship with Gold mineralization. *Earth Science-Journal of China University of Geosciences*, *22*, 20–26. (in Chinese with English abstract).

Zhou, X. M., Shen, W. Z., Shu, L. S., & Niu, Y. L. (2006). Petrogenesis of mesozoic granitoids and volcanic rocks in South China: A response to tectonic evolution. *Episodes*, *29*, 26–33.

Zhou, Y. Z., Zeng, C. Y., Li, H. Z., An, Y. F., Liang, J., & Lu, W. C. (2012). Geological evolution and ore-prospecting targets in southern segment of Qinzhou Bay-Hangzhou Bay juncture orogenic belt, Southern China. *Geological Bulletin of China*, *31*, 486–491. (in Chinese with English abstract).

Zhou, Y. Z., Zhang, H. H., Lu, H. Z., Guha, J., & Chown, E. H. (1995). Fluid inclusions and hydrothermal fluids of Hetai gold deposit, Western Guangdong, China. *Acta Mineralogica Sinica*, *15*, 411–417. (in Chinese with English abstract).

Zhu, B., Zhang, J., Tu, X., Chang, X., Fan, C., Liu, Y., & Liu, J. (2001). Pb, Sr, and Nd isotopic features in organic matter from China and their implications for petroleum generation and migration. *Geochimica et Cosmochimica Acta*, *65*, 2555–2570.

How to cite this article: Wang L, Zhao Z, Huang Q, et al. The genesis of gold deposits in the Hetai goldfield, South China: New constraints from geochronology, fluid inclusion, and multiple isotopic studies. *Geological Journal*. 2020;55:2447–2472. https://doi.org/10.1002/gj.3516